Molecular Cell

Article

Functional nutrient-genetic profiling reveals biotin and FBXW7 are essential to bypass glutamine addiction

Graphical abstract

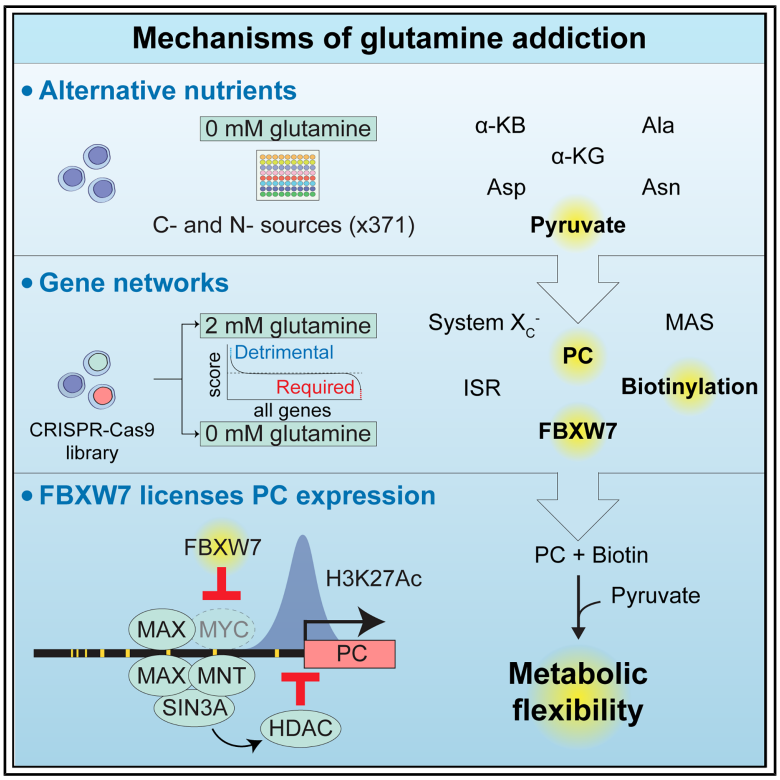

Highlights

- Nutrient-genetic screens identify mechanisms determining glutamine addiction
- Biotinylation licenses anaplerosis upon glutamine depletion
- FBXW7 promotes pyruvate-mediated growth of glutamine-starved cells
- The MYC extended network represses PC transcription via MNT/SIN3A and deacetylation

Authors

Miriam Lisci, Fanny Vericel, Yifan Liu, Hector Gallart-Ayala, Julijana Ivanisevic, Owen S. Skinner, Alexis A. Jourdain

Correspondence

alexis.jourdain@unil.ch

In brief

Lisci et al. present a unified model revealing how cells escape glutamine addiction, a metabolic vulnerability of several cancers. Combining systematic genetic and nutrient screens, they show that biotin and the tumor suppressor FBXW7 enable metabolic flexibility by sustaining mitochondrial pyruvate carboxylation, with FBXW7 acting upstream of MYC-mediated transcriptional regulation.

Lisci et al., 2026, Molecular Cell *86*, 1–16
March 5, 2026
https://doi.org/10.1016/j.molcel.2026.02.002

CellPress

Molecular Cell

CellPress
OPEN ACCESS

Article

Functional nutrient-genetic profiling reveals biotin and FBXW7 are essential to bypass glutamine addiction

Miriam Lisci,[1] Fanny Vericel,[1] Yifan Liu,[2] Hector Gallart-Ayala,[3] Julijana Ivanisevic,[3] Owen S. Skinner,[2] and Alexis A. Jourdain[1,4,*]

[1]Department of Immunobiology, Faculty of Biology and Medicine, University of Lausanne, 1066 Epalinges, Switzerland
[2]Department of Chemistry and Chemical Biology, Northeastern University, Boston, MA 02115, USA
[3]Metabolomics Platform, Faculty of Biology and Medicine, University of Lausanne, 1005 Lausanne, Switzerland
[4]Lead contact
*Correspondence: alexis.jourdain@unil.ch
https://doi.org/10.1016/j.molcel.2026.02.002

SUMMARY

Metabolic flexibility is key to survival and growth in all living organisms. In mammals, the pathways supporting cell proliferation in nutrient-limiting conditions have not been fully elucidated, although certain tumors display metabolic dependencies that can be targeted for therapy. Here, we combine metabolic tracers, nutrient supplementation, and genome-wide CRISPR-Cas9 screening to investigate the pathways mediating glutamine addiction, a hallmark of several cancers. We report that the vitamin biotin allows the bypassing of glutamine dependence by activating pyruvate carboxylase (PC), and we discover a mechanism by which the tumor suppressor FBXW7 promotes pyruvate anaplerosis. Mechanistically, we show that FBXW7 prevents c-MYC accumulation and recruitment of a cluster of transcriptional repressors, including MAX, MNT, and SIN3A, to the *PC* promoter, thereby maintaining *PC* expression and avoiding glutamine addiction. Our work sheds light on the molecular mechanisms that support metabolic flexibility and prevent glutamine addiction in cancer, with high relevance for *FBXW7*-associated cancer mutations.

INTRODUCTION

All life forms have evolved to cope with varying environments. In humans, malnutrition, infection, or tumorigenesis can perturb access to nutrients, making metabolic flexibility crucial to ensure viability.[1] Amino acids are some of the nutrients that show the highest variation in our diet and across tissues.[2] Among them, glutamine is the most abundant amino acid in plasma and one of the most highly utilized by cells in culture.[3,4] Besides its role as an essential constituent of proteins, glutamine acts as a major contributor to the tricarboxylic acid (TCA) cycle, participating in ATP generation and amino acid synthesis, and to nitrogen metabolism, serving as an amine donor in multiple metabolic reactions, including nucleotide metabolism. The relative contribution of glutamine to the carbon and nitrogen cellular pools, and how they are shaped by local nutrient availability, remains incompletely understood.

While glutamine is classically viewed as a non-essential amino acid, it has long been known that mammalian cells can become dependent on its extracellular availability.[4] This phenomenon, referred to as "glutamine addiction," has been observed both in cell culture and *in vivo*, and it is thought to result from high proliferation rates exceeding the capacity for intracellular biosynthesis.[5] However, it remains unclear whether glutamine addiction results from a scarcity of carbon or nitrogen. Glutamine metabolism plays a crucial role in cancer proliferation, and glutamine addiction is a hallmark of certain cancers,[6,7] together with the expression of the oncogene *MYC*, which encodes the transcription factor c-MYC and induces the upregulation of several transporters and glutamine-related enzymes, including glutaminase.[8–11] Notably, *in vivo* studies showed remarkable differences in glutamine consumption and abundance across tumor types,[12–14] increasing the complexity of glutamine addiction in cancer. Understanding which molecular mechanisms and nutrients modulate survival in a glutamine-limited environment could guide novel approaches to limit cancer proliferation.

Earlier studies have highlighted metabolic pathways sustaining the proliferation of glutamine-deprived cells, including pyruvate carboxylation, the malate-aspartate shuttle (MAS), and asparagine synthesis,[15–17] as well as others that become detrimental upon glutamine restriction, such as proline synthesis.[18] Despite this important work, we still lack a global, systematic view of the nutrients and pathways involved in cell survival when glutamine is scarce. Here, we combine metabolic tracing with large-scale nutrient and genome-wide genetic screening to provide a unified model of the metabolites and molecular

pathways at play in glutamine addiction. We report that biotin licenses proliferation of glutamine-deprived cells by promoting the activity of pyruvate carboxylase (PC), and we further identify an epigenetic mechanism whereby the tumor suppressor *FBXW7* regulates glutamine addiction by promoting expression of *PC*. We show that FBXW7 acts upstream of the MYC extended network, a cluster of transcriptional modulators including repressor proteins that mediate histone deacetylation. We report that *FBXW7* depletion leads to c-MYC accumulation, recruitment of MAX, MNT, and SIN3A to the *PC* promoter, and reduced H3K27 acetylation. Thus, FBXW7 inhibits transcriptional repressor recruitment, licensing *PC* expression, pyruvate anaplerosis, and proliferation in glutamine-limiting conditions.

RESULTS

Systematic investigation of glutamine addiction

To identify the molecular mechanisms underlying glutamine addiction, we investigated the metabolic reactions that involve glutamine (ChEBI: 28300) and glutamine-derived glutamate (ChEBI: 14321) in humans. Among the 20,420 reviewed protein-coding genes from the UniProt 2025 Reviewed database,[19] we found 43 and 127 proteins using glutamine and glutamate, respectively (Figure 1A; Table S1). These proteins mainly encode for metabolic enzymes, transporters, and glutamate receptors, and among them, 28 glutamine-related and 68 glutamate-related proteins are expressed in human K562 myelogenous leukemia cells (transcripts per million, TPM > 1) (Table S1).

Given the multiple biosynthetic pathways in which glutamine is involved by contributing both carbon and nitrogen groups,[20] we performed a time-resolved metabolic tracer analysis in K562 using uniformly labeled ^{13}C-glutamine and ^{15}N-glutamine to measure the participation of glutamine in cellular carbon and nitrogen pools, respectively (Figures 1B, 1C, S1A, and S1B; Table S2). We found that glutamine-derived carbon participates in most of the carbon pools of amino acids, such as glutamate, aspartate, and asparagine, and in glutamate-derived TCA cycle intermediates, including α-ketoglutarate (α-KG), succinate, malate, and citrate, reaching >85% labeling after 8 h. Glutamine-derived carbon was also incorporated at a similar, yet slower rate in pyrimidines (UMP) and pyrimidine-derived metabolites in the hexosamine biosynthetic pathway (UDP-GlcNAc) but not in purines (IMP and AMP), which mostly contain glucose-derived carbons. By contrast, glutamine-derived nitrogen showed a more heterogeneous pattern, and while purines and pyrimidines reached >60% labeling after 8 h, amino acids such as glutamate and aspartate only reached partial ^{15}N-labeling (<50%), indicating significant participation of additional nitrogen sources beyond glutamine. An exception was asparagine, which contains an extra glutamine-derived nitrogen and showed >85% ^{15}N-labeling within 2 h. By contrast, we observed no ^{13}C labeling in pyruvate or acetyl-CoA, suggesting no malic enzyme activity in K562, in contrast to other cells[21,22] (Figure S1B).

We next explored whether glutamine addiction could be rescued by the addition of carbon or nitrogen sources. We first tested the ability of K562 to grow in the absence of glutamine and found that it led to a rapid loss of proliferation and viability, indicating strong glutamine addiction (Figures 1D and S1C). We then designed an unbiased nutrient screen comparing the effect of 371 carbon and nitrogen sources, many of which are present in the circulation or in the tumor microenvironment,[12,23] on restoring proliferation in glutamine-limited conditions (Figure 1E). We identified a wide range of carbon sources, including carboxylic acids such as pyruvate, α-KG, and α-ketobutyrate (α-KB), some of which had previously been observed in the context of glutamine deprivation,[24] glutaminase inhibition,[15] and mitochondrial dysfunction[25,26] (Figure 1F; Table S3). We also identified metabolites that could act as both carbon and nitrogen donors, including alanine and alanine-containing dipeptides, which can be deaminated to pyruvate by alanine aminotransferase.[27] In general, we observed that proliferation increased the most upon addition of carboxylic acids, compared with nitrogen donors (Figures 1G and 1H), consistent with the more limited glutamine contribution to the nitrogen pool in our tracer analysis. Together, our results in K562 indicate that glutamine addiction results mainly from the need for carbon rather than nitrogen.

Anaplerosis, rather than redox imbalance, is the cause of glutamine addiction

To better characterize the metabolome of cells cultured in the presence or absence of glutamine, we performed steady-state metabolomics in glutamine-deprived cells. We found decreased abundance of all TCA cycle intermediates, as well as amino acids such as glutamate, aspartate, and asparagine, which we confirmed using MetaboAnalyst pathway analysis[28] (Figure 2A; Table S4). The levels of metabolites related to glycolysis, nucleotide synthesis, the pentose phosphate pathway, and other amino acids showed little to no variation in the absence of glutamine. Based on the key role of carbon supplementation (Figure 1), we investigated whether the addition of the carbon sources identified in our screen could rescue the abundance of metabolites found to be depleted in glutamine-limited conditions. We selected pyruvate as a carboxylic acid that is not directly downstream of glutamine, that does not contain a nitrogen group, and that showed the most beneficial impact on cell proliferation in glutamine-limited conditions in our nutrient screen (Figures 1F–1H). We observed that pyruvate could restore the levels of most metabolites depleted in the absence of glutamine, including TCA cycle intermediates, glutamate, glutamine, aspartate, and asparagine (Figure 2A; Table S4).

These results suggested that pyruvate promotes the proliferation of glutamine-starved cells through anaplerosis, and to exclude a role for exogenous pyruvate in NAD$^+$ regeneration,[25,29] we measured the NADH/NAD$^+$ ratio in glutamine-deprived K562 and compared the effect of pyruvate to that of *Lb*NOX, an enzyme prosthetic used as an NADH oxidase.[30] We found that glutamine starvation increases the NADH/NAD$^+$ ratio (Figure S2A), in contrast to previous work,[31] but as expected from lower TCA cycle activity in glutamine-deprived conditions. We corrected this imbalance by supplementing pyruvate, which performed better than *Lb*NOX in promoting the proliferation of glutamine-starved cells (Figure S2B). Therefore, we conclude that the ability of pyruvate to rescue proliferation under glutamine-deprived conditions is not primarily via restoring NADH/NAD$^+$ balance.

Please cite this article in press as: Lisci et al., Functional nutrient-genetic profiling reveals biotin and FBXW7 are essential to bypass glutamine addiction, Molecular Cell (2026), https://doi.org/10.1016/j.molcel.2026.02.002

CellPress
OPEN ACCESS

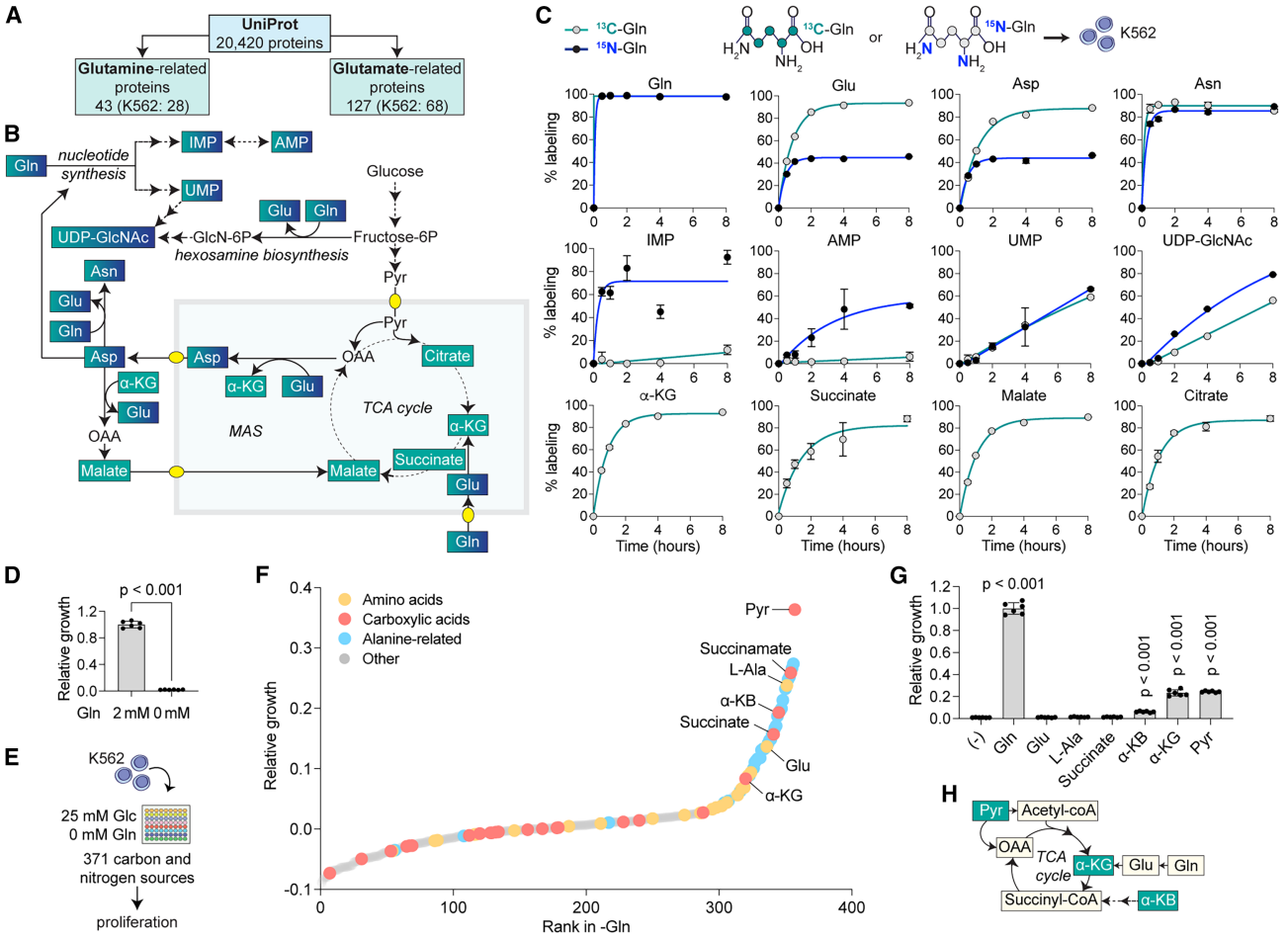

Figure 1. Systematic investigation of glutamine addiction using isotope tracing and nutrient screening

(A) Human protein-coding genes involving glutamine or glutamate (UniProt). Genes expressed in K562 are in parentheses.

(B) Metabolic pathways analyzed by U-^{13}C and U-^{15}N Gln (glutamine) tracing in K562. Analyzed metabolites are highlighted in green (carbon sources) or in both green and blue (carbon and nitrogen sources). Light blue box, mitochondrion; yellow ellipses, mitochondrial transporters. Multiple enzymatic steps, multiple arrows and dotted lines. α-KG, α-ketoglutarate; Asn, asparagine; Asp, aspartate; Glu, glutamate; MAS, malate-aspartate shuttle; OAA, oxaloacetate; Pyr, pyruvate; UDP-GlcNAc, uridine diphosphate N-acetylglucosamine; UMP, IMP, and AMP, uridine, inosine, and adenosine monophosphate.

(C) Total ^{13}C-Gln and ^{15}N-Gln incorporation in amino acids, nucleotides, UDP-amino sugar UDP-GlcNAc, and TCA cycle intermediates in K562.

(D) Proliferation (Prestoblue) of K562 in medium with or without glutamine. Values represent relative growth compared with cell proliferation in 2 mM glutamine. *p* values, unpaired *t* test.

(E) Representation of nutrient screen in glutamine-starved K562.

(F) Screen results highlighting nutrients promoting K562 proliferation in glutamine-deprived medium. Glutamine and glutamine-containing dipeptides are not shown.

(G) Validation of selected nutrients (2 mM) in glutamine-starved K562. Relative growth is compared with cell proliferation in non-supplemented (-) medium. L-Ala, L-alanine; succinate, diethyl succinate; α-KB, α-ketobutyrate; α-KG, α-ketoglutarate (dimethyl 2-oxoglutarate).

(H) Schematic representation of the role of pyruvate, α-KG, and α-KB in anaplerosis. All data are represented as mean ± SD, with the addition of fitted curves in (C). *p* values, one-way ANOVA. Only *p* values < 0.05 are shown.

See also Figure S1 and Tables S1–S3.

To further validate the anaplerotic route, we supplemented pyruvate to K562 cultured in the absence of glutamine and found that this was sufficient to increase proliferation (Figure 2B). This effect was driven by pyruvate entry into the mitochondria, consistent with the increased abundance of TCA cycle intermediates and confirmed by pharmacological inhibition of the mitochondrial pyruvate carrier (UK5099), which ablated pyruvate-mediated proliferation in glutamine-deprived medium (Figure 2C). We next sought to validate whether pyruvate supports proliferation through anaplerosis and performed a ^{13}C-labeled pyruvate tracer analysis in glutamine-deprived K562 (Figures 2D and 2E; Table S5) and in primary murine CD8^{+} T cells (Figures S2C and S2D; Table S5). We observed ^{13}C enrichment in most TCA cycle intermediates and TCA-derived amino acids in both glutamine-rich and glutamine-deprived conditions. However, ^{13}C enrichment increased upon glutamine

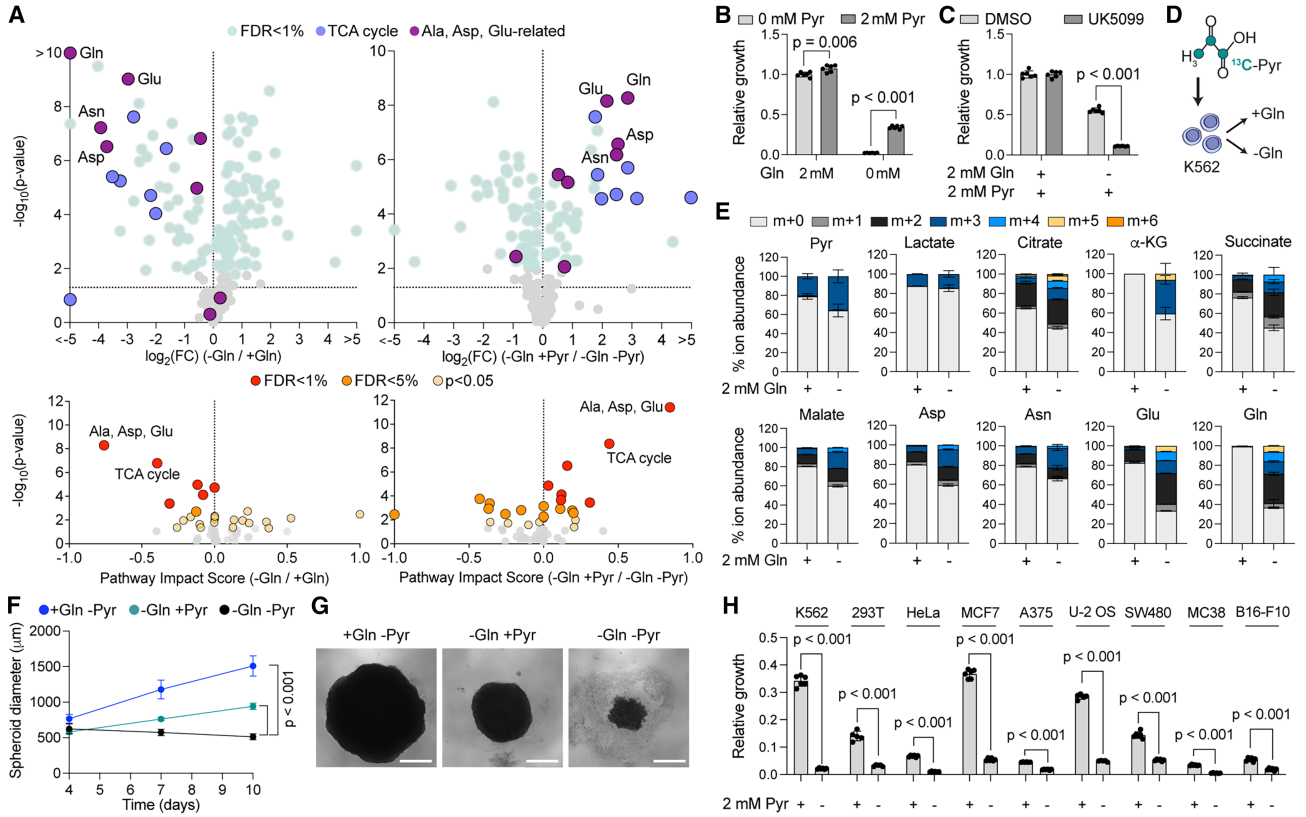

Figure 2. Metabolomics and proliferation analyses of glutamine-deprived cells

(A) Top, metabolite abundance in K562 cultured in glutamine (Gln)-deprived vs. glutamine-rich medium (left) or with pyruvate (Pyr) supplementation in glutamine-free conditions (right). TCA intermediates and metabolites related to alanine (Ala), glutamate (Glu), aspartate (Asp), and asparagine (Asn) are labeled. Bottom, MetaboAnalyst Pathway Analysis of significantly altered metabolites in glutamine-deprived vs. glutamine-rich medium (left) or with pyruvate supplementation in glutamine-free conditions (right). FDR, Benjamini-Hochberg false discovery rate correction. FC, fold change.

(B) Proliferation of K562 supplemented with pyruvate, with or without glutamine. Relative growth: fold change of cells cultured in 2 mM glutamine with no pyruvate.

(C) Proliferation of control (DMSO) or UK-5099-treated K562 upon pyruvate addition, with or without glutamine. Relative growth: fold change of proliferation of control cells supplemented with glutamine and pyruvate.

(D) ^{13}C-pyruvate tracing in K562.

(E) Metabolites enriched in ^{13}C-pyruvate in glutamine-rich or -deprived medium (relative isotopolog fractions). α-KG, α-ketoglutarate.

(F and G) Diameter of 293T spheroids cultured in medium supplemented with glutamine or pyruvate (F) and representative images (day 10 post-seeding) (G). Scale bar, 500 μm.

(H) Growth assay of human (K562, 293T, HeLa, MCF7, A375, U-2 OS, and SW480) and murine (MC38, B16-F10) cell lines in the absence of glutamine, supplemented with pyruvate where indicated. Relative growth is calculated as the fold change of proliferation in the glutamine-rich medium of each cell line. All data are represented as mean ± SD. *p* values, multiple unpaired *t* tests. Only *p* values < 0.05 are shown.

See also Figure S2 and Tables S4 and S5.

depletion, indicating that cells increase the use of pyruvate for anaplerosis when glutamine is scarce.

To confirm that the role of pyruvate in supporting proliferation of glutamine-starved cells was not cell type-specific, we used HEK239T (293T) spheroids as an alternative 3D model to measure cell proliferation. We found that the addition of pyruvate to the cell culture medium was sufficient to increase proliferation of glutamine-depleted 293T spheroids (Figures 2F and 2G), a result that we further validated across seven additional human and murine cancer cell lines (Figure 2H). Together, our findings confirmed that carbons from pyruvate promote proliferation of glutamine-restricted cells via anaplerosis and that pyruvate-mediated proliferation in glutamine-deprived medium is generalizable across cell lineages, offering a unique opportunity to further study the mechanism of glutamine addiction.

A unified model of glutamine addiction from genome-wide CRISPR-Cas9 screening

We next designed a genome-wide screen aimed at identifying the molecular pathways able to maintain proliferation in glutamine-free, pyruvate-rich conditions. We infected K562 with the Brunello lentiviral genome-wide CRISPR-Cas9 library and transferred cells to a DMEM-based medium containing glucose and pyruvate, either with or without glutamine. After 21 days, we harvested cells and performed next-generation sequencing to determine the abundance of single guide

Please cite this article in press as: Lisci et al., Functional nutrient-genetic profiling reveals biotin and FBXW7 are essential to bypass glutamine addiction, Molecular Cell (2026), https://doi.org/10.1016/j.molcel.2026.02.002

CellPress
OPEN ACCESS

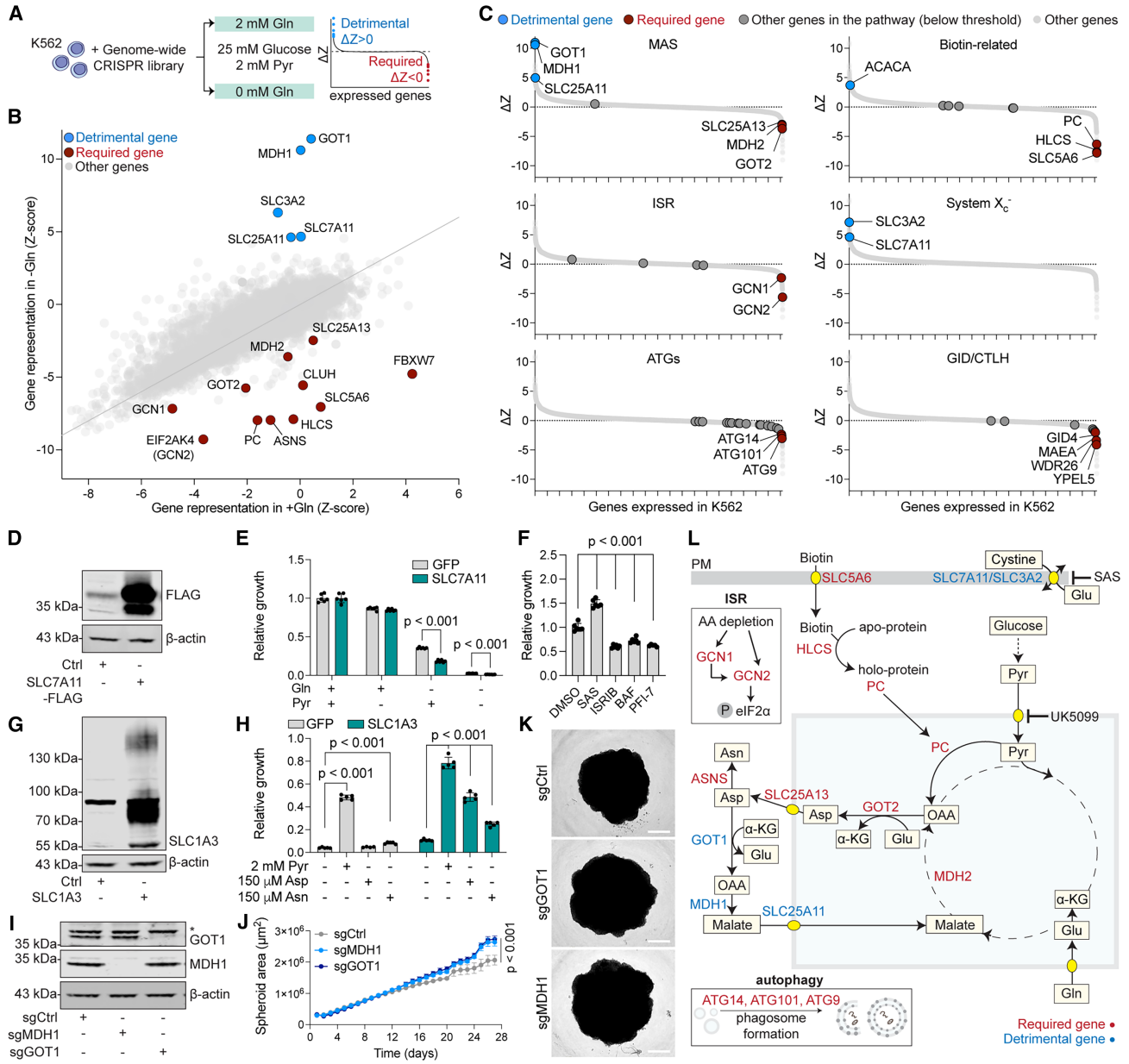

Figure 3. Genome-wide screening provides a unified model of pathways determining glutamine addiction

(A) Genome-wide CRISPR-Cas9 screening in K562 cultured in medium containing pyruvate (Pyr), with or without glutamine (Gln).

(B) CRISPR-Cas9 screen identifying genes required (red) or detrimental (blue) for K562 proliferation in glutamine-deprived medium supplemented with pyruvate.

(C) Gene essentiality score ($\Delta Z = Z_{-Gln} - Z_{+Gln}$) for selected pathways in K562. MAS, malate-aspartate shuttle; ISR, integrated stress response; ATGs, autophagy genes; GID/CTLH, genes related to the GID/CTLH (C-terminal to LisH) E3 ligase complex. Dotted line, $\Delta Z = 0$ (no difference between +Gln and -Gln). Individual genes are labeled as red (required for proliferation of glutamine-starved cells, $\Delta Z < -2$), blue (detrimental for proliferation, $\Delta Z > 2$), or gray dots (below threshold).

(D and E) K562 overexpressing the system X_c^- subunit SLC7A11 or GFP control (Ctrl) (D) cultured in medium enriched with glutamine or pyruvate (E). Relative growth is calculated in comparison to cells supplemented with both glutamine and pyruvate. *p* values, multiple unpaired *t* tests.

(F) Proliferation of glutamine-starved K562 treated with inhibitors of the X_c^- antiporter (sulfasalazine [SAS]), the ISR (ISRIB), autophagy (bafilomycin [BAF]), and the GID/CTLH complex (PFI7). Relative growth is calculated in comparison to untreated cells (DMSO). *p* values, one-way ANOVA.

(G and H) K562 expressing the plasma membrane amino acid transporter SLC1A3 or GFP control (G) cultured in glutamine-deprived medium supplemented with pyruvate, aspartate (Asp), or asparagine (Asn) (H). Relative growth was calculated for each sample by comparison with non-supplemented medium. *p* values, one-way ANOVA.

(legend continued on next page)

Please cite this article in press as: Lisci et al., Functional nutrient-genetic profiling reveals biotin and FBXW7 are essential to bypass glutamine addiction, Molecular Cell (2026), https://doi.org/10.1016/j.molcel.2026.02.002

RNAs (sgRNAs) in each condition. We analyzed the data using a *Z* score-based method[26] to calculate the essentiality of each gene, highlighting genes that were required ($\Delta Z < 0$) or detrimental ($\Delta Z > 0$) for the growth of glutamine-starved cells (Figures 3A and S3A; Table S6).

Validating the robustness of our genome-wide approach, our screen re-identified several factors known to influence the survival of cells in the absence of glutamine, either by promoting or inhibiting proliferation. These include the mitochondrial arm of the MAS[24,32] involved in aspartate synthesis (*GOT2*, *MDH2*, and *SLC25A13*); *PC*, which converts pyruvate to oxaloacetate, thus playing an important role in anaplerosis in cancer cells[15,33]; the provision of asparagine[16,17] via asparagine synthase (*ASNS*); the amino acid-sensing arm of the integrated stress response (ISR) (*GCN1* and *GCN2*)[34]; and the plasma membrane cystine-glutamate exchanger system X_c^- (*SLC3A2* and *SLC7A11*),[35,36] which lies downstream of the ISR[37] (Figures 3B and 3C). Our screen also identified individual genes and pathways not previously linked to glutamine addiction, including biotin-related genes (*SLC5A6* and *HLCS*)[38–41]; a cytosolic protein involved in the translation of mitochondria-targeted proteins (*CLUH*)[42]; autophagy-related genes (*ATG*s), as well as ubiquitination-related pathways, including the GID/CTLH complex (*GID4*, *MAEA*, *WDR26*, and *YPEL5*)[43,44]; and a substrate recognition component of the Skp1-Cullin-F-box (SCF) E3 ligase (*FBXW7*),[45] all of which were required to survive glutamine starvation. Malic enzymes (*ME1* and *ME2*) did not score in our screen, likely because of the exogenous pyruvate available in the medium (Figure S3B).

We validated these hits using genetic and pharmacological tools, first by assessing the contribution of system X_c^- and its subunit SLC7A11. Glutamine depletion induced upregulation of ATF4, a known marker of the ISR,[34] and of SLC7A11. Notably, we found that pyruvate supplementation partially normalized both ATF4 and SLC7A11 expression in glutamine-deprived cells (Figure S3C). Next, we validated the detrimental role of system X_c^- in glutamine-deprived conditions, as highlighted by our screen. We show that overexpression of *SLC7A11* decreased growth of glutamine-starved cells (Figures 3D and 3E), while inhibition of system X_c^- by sulfasalazine (SAS) promoted proliferation in the same conditions (Figure 3F). These results corroborate previous findings[36] and likely hint at a detrimental effect for glutamate export by system X_c^- in glutamine-deprived cells.

Next, we used pharmacological inhibition of the ISR (ISRIB), autophagy (bafilomycin [BAF]), and the glucose-induced degradation-deficient (GID), also referred to as the C-terminal to LisH (CTLH) E3 ligase complex (PFI7[46]), and showed that inhibition of these pathways decreased proliferation upon glutamine depletion, despite pyruvate addition, confirming their necessity as highlighted by our screen (Figure 3F). We further corroborated the validity of our model by overexpressing the glutamate-aspartate transporter *SLC1A3* and supplementing glutamine-deprived cells with aspartate or asparagine. This approach was previously used to highlight the importance of pyruvate for aspartate synthesis[17,29] and for aspartate in promoting proliferation of glutamine-starved cells,[24,32] and we confirmed it partially rescued the growth of glutamine-starved K562 (Figures 3G and 3H).

Curiously, the main factors whose depletion promoted the proliferation of cells in glutamine-limited conditions were part of the cytosolic arm of the MAS (*GOT1*, *MDH1*, and *SLC25A11*), which mirrors the mitochondrial arm (*GOT2*, *MDH2*, and *SLC25A13*) by bringing aspartate-derived carbon back to mitochondria. *GOT1* and *MDH1* are well-characterized for their role in oxidative stress, affecting the growth of cancers such as pancreatic ductal adenocarcinoma.[47,48] While higher expression of these genes correlates with poor prognosis in some cancers,[49,50] both our screen and validation in 293T spheroids showed that depletion of *GOT1* or *MDH1* promoted proliferation in glutamine-limited conditions, possibly by preventing re-entry of carbon intermediates in mitochondria and maintaining aspartate in the cytosol (Figures 3I–3K).

Overall, our genetic and nutrient screens highlight genes and nutrients participating in interconnecting pathways and, together with earlier literature, point to a unified model where glutamine-restricted cells rely on pyruvate import into mitochondria, conversion to oxaloacetate, mitochondrial aspartate synthesis, and its export to the cytosol via the MAS (Figure 3L). Intriguingly, we show that blocking the return of aspartate to mitochondria by inhibiting the cytosolic arm of the MAS is beneficial in the context of glutamine restriction and spheroid growth. This further confirms a strong need for cytosolic aspartate, where it can serve as a substrate for both protein and nucleotide synthesis and for asparagine. In addition, our screen also recovered satellite pathways such as the ISR and glutamate export by the system X_C^- and importantly highlighted biotin metabolism and *FBXW7*, not previously linked to glutamine addiction.

Biotin metabolism promotes growth in glutamine-limited conditions

Biotin, also known as vitamin B7 or H, is the substrate for biotinylation, a post-translational modification that occurs in mitochondrial carboxylases (PC, MCCC1/MCCC2, and PCCA/PCCB) and in the cytosolic acetyl-CoA carboxylase (ACACA/ACACB). Our screen identified the biotin plasma membrane transporter (*SLC5A6*) and the biotin conjugating enzyme (*HLCS*) as required for cell proliferation in the absence of glutamine (Figure 4A). Notably, while human cells encode four classes of biotin-dependent carboxylases, only *PC* was essential for the growth of cells in glutamine-deprived conditions (Figures 3B and 3C). To validate these hits, we depleted their expression using CRISPR-Cas9 and observed a strong reduction in the ability of K562 to survive glutamine deprivation (Figure 4B). Similarly, we found that K562 cells and 293T spheroids required both biotin and pyruvate for growth (Figures 4C–4E) and confirmed that

(I–K) 293T depleted of the MAS proteins GOT1 (sgGOT1) or MDH1 (sgMDH1) (I) cultured as 3D spheroids in glutamine-deprived medium supplemented with pyruvate (J, K). * = non-specific band. Representative images for 293T spheroids (K) 26 days post-seeding. Scale bar, 500 μm. *p* values, one-way ANOVA. (L) Unified model of networks modulating proliferation in glutamine-deprived medium. Light blue box, mitochondrion; yellow ellipses, mitochondrial transporters. PM, plasma membrane. α-KG, α-ketoglutarate; Glu, glutamate; OAA, oxaloacetate. All data are represented as mean ± SD. Only p values < 0.05 are shown. See also Figure S3 and Table S6.

Please cite this article in press as: Lisci et al., Functional nutrient-genetic profiling reveals biotin and FBXW7 are essential to bypass glutamine addiction, Molecular Cell (2026), https://doi.org/10.1016/j.molcel.2026.02.002

CellPress
OPEN ACCESS

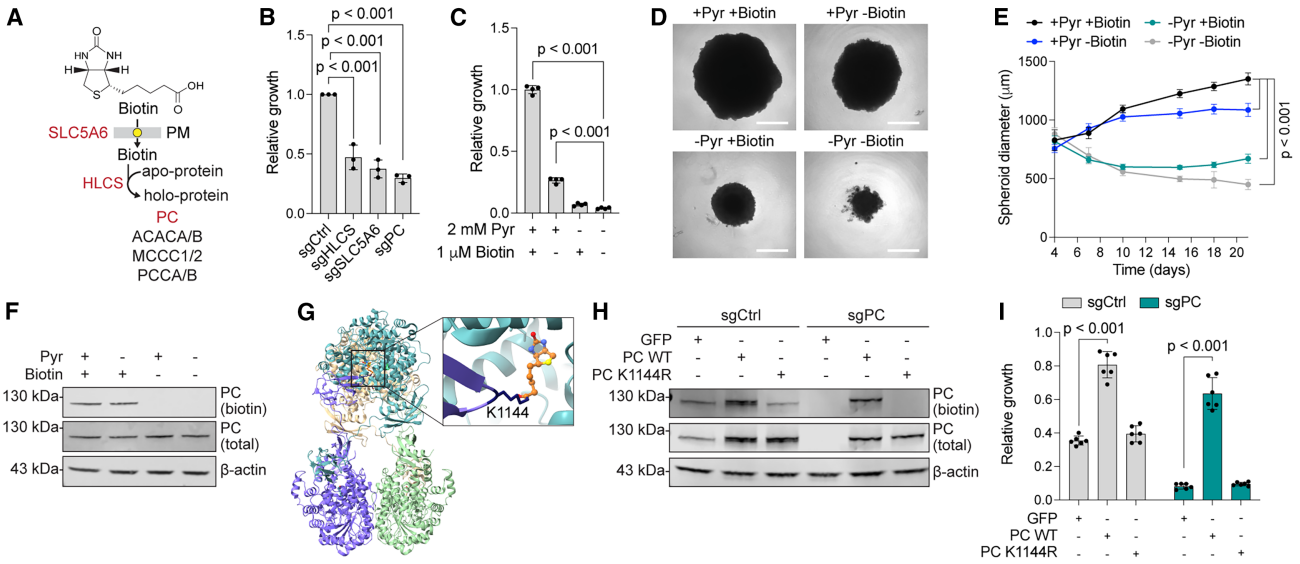

Figure 4. Biotin licenses glutamine-independent growth by promoting PC activity

(A) Biotin-related genes required (red) in glutamine-deprived medium.

(B) Proliferation of glutamine-starved K562 depleted of biotin-related genes. All conditions were supplemented with 2 mM pyruvate. Relative growth: fold change of sgCtrl.

(C) Proliferation of WT K562 cultured in glutamine-deprived medium upon addition of pyruvate (Pyr), biotin, or both. Relative growth: fold change of proliferation in medium supplemented with both pyruvate and biotin.

(D and E) Representative images (20 days post-seeding) (D) and spheroid diameter (E) of glutamine-restricted 293T supplemented with biotin, pyruvate, or both. Scale bar, 500 μm.

(F) Total protein expression and biotinylation of pyruvate carboxylase (PC) in medium supplemented with, or deprived of, pyruvate and biotin.

(G) Structure of human PC tetramer (2.61 Å, PDB: 8XL9). Each monomer is represented in a different color. The inset shows one biotin ligand (orange) and biotin-binding site (K1144, purple) among the four biotin-binding sites in the tetramer.

(H and I) Control (sgCtrl) and *PC*-deficient K562 (sgPC) overexpressing WT PC, K1144R mutant PC, or GFP control (H) cultured in glutamine-depleted, pyruvate-supplemented medium (I). Values represent the relative growth of each sample in comparison to proliferation in a glutamine-rich medium. All data are represented as mean ± SD. All *p* values, one-way ANOVA. Only *p* values < 0.05 are shown.

the depletion of either did not affect PC stability (Figure 4F), pointing to a specific functional requirement for biotinylation.

To test whether PC biotinylation is required for bypassing glutamine addiction, we searched structural databases to identify the biotinylated residue in human PC, which pointed us to lysine 1144 (PDB: 8XL9)[51] (Figure 4G). We generated a PC point mutant that cannot be biotinylated (K1144R) and confirmed that wild-type (WT) and K1144R PC were expressed at similar levels and that PC stability was not affected by the lack of biotinylation (Figure 4H). Next, we performed a growth assay to test whether PC biotinylation promoted the proliferation of glutamine-starved cells. While we found that overexpression of WT PC was sufficient to rescue the proliferation of glutamine-starved *PC*-depleted cells and even promoted the proliferation of *PC*-competent cells in the same conditions, PC K1144R-expressing cells failed to grow upon glutamine deprivation (Figure 4I). Together, our data indicate that biotinylation of PC is required to support proliferation in glutamine-limited conditions and that biotinylated PC is a limiting factor for the growth of glutamine-addicted cells.

FBXW7 supports PC expression and pyruvate anaplerosis

The gene that scored as the most required factor in the absence of glutamine was the tumor suppressor *FBXW7*, which, in contrast to most other hits in our genetic screen, is not known to be involved in central carbon metabolism (Figures 3B and S3B). FBXW7 is a well-characterized substrate recognition component for the cytosolic SKP1-CUL1-F-box E3 ubiquitin ligase complex, involved in the degradation of the protein products of oncogenes such as c-MYC, c-JUN, and cyclin E.[52–55]

Since a role for *FBXW7* in central carbon metabolism was unexpected, we depleted *FBXW7* in K562 using CRISPR-Cas9 (Figure 5A) and measured proliferation in glutamine-deprived medium upon supplementation with carbon sources (Figures 5B and 5C). We observed that while *FBXW7*-depleted cells showed no proliferation defects in a glutamine-rich medium, they grew more slowly in the absence of glutamine, despite the addition of pyruvate. To investigate whether this difference was specifically due to pyruvate metabolism, we supplemented the cell medium with a membrane-permeable α-KG (dimethyl 2-oxoglutarate) analog and found that it was able to promote cell proliferation independently of the expression of *FBXW7*, pointing to a defect in pyruvate anaplerosis, rather than a global defect in central carbon metabolism. Similarly, *FBXW7*-depleted 293T spheroids failed to grow in glutamine-free conditions, even after pyruvate supplementation (Figures 5D and 5E). To clarify the fate of pyruvate in *FBXW7*-

Please cite this article in press as: Lisci et al., Functional nutrient-genetic profiling reveals biotin and FBXW7 are essential to bypass glutamine addiction, Molecular Cell (2026), https://doi.org/10.1016/j.molcel.2026.02.002

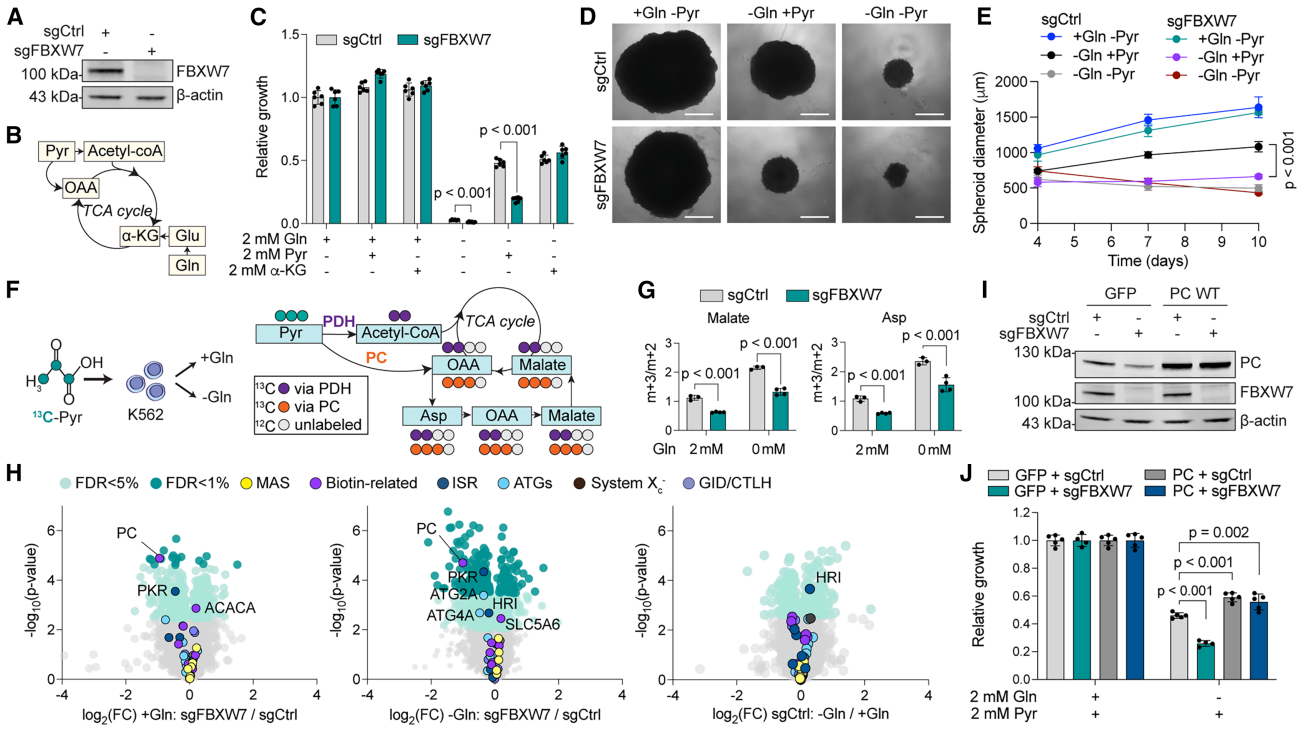

Figure 5. FBXW7 mediates pyruvate anaplerosis by promoting PC expression

(A) FBXW7 expression in control (sgCtrl) and *FBXW7*-depleted (sgFBXW7) K562.

(B) Simplified model showing sources of carbon entry into the TCA cycle. α-KG, α-ketoglutarate; Gln, glutamine; Glu, glutamate; OAA, oxaloacetate; Pyr, pyruvate.

(C) Proliferation of control and *FBXW7*-depleted cells in media supplemented with glutamine, pyruvate, or α-KG. *p* values, multiple unpaired *t* tests.

(D and E) Representative images (20 days post-seeding) (D) and spheroid diameter (E) of control and *FBXW7*-depleted 293T supplemented with glutamine or pyruvate. Scale bar, 500 μm. *p* values, multiple unpaired *t* tests.

(F) Representation of ^{13}C-pyruvate tracing in K562.

(G) m+3/m+2 ratio of ^{13}C-pyruvate-derived carbons for malate and aspartate (Asp) in control and *FBXW7*-depleted cells cultured in glutamine-rich or -deprived medium.

(H) Differential protein expression in glutamine-rich (left) and glutamine-deprived (center) *FBXW7*-depleted K562 compared with WT controls, and in control cells only upon culture in glutamine-rich versus glutamine-depleted medium (right). FC, fold change. FDR, Benjamini-Hochberg false discovery rate correction. MAS, malate-aspartate shuttle; ISR, integrated stress response; ATGs, autophagy genes; GID/CTLH, genes related to the GID/CTLH (C-terminal to LisH) E3 ligase complex.

(I and J) Control and *FBXW7*-deficient K562 overexpressing WT PC or GFP control (I) cultured in pyruvate-enriched medium supplemented with or deprived of glutamine (J). Values represent the relative growth of each sample in comparison to proliferation in a glutamine-rich medium. All data are represented as mean ± SD. *p* values, one-way ANOVA. Only *p* values < 0.05 are shown.

See also Figure S4 and Tables S7 and S8.

depleted cells, we repeated our ^{13}C-pyruvate tracer experiment and focused on malate and aspartate, whose relative fractions of m+3 isotopolog increased in glutamine-limited conditions (Figure 2E). This was indicative of PC-mediated conversion of pyruvate into oxaloacetate, as opposed to m+2 isotopologs, which are generated by pyruvate dehydrogenase (PDH)-mediated conversion of pyruvate into acetyl-CoA. While we confirmed increased enrichment in m+3 isotopologs in the absence of glutamine, we found it to be significantly reduced in *FBXW7*-depleted cells, irrespective of the presence of glutamine, further suggesting impaired pyruvate anabolism via PC (Figures 5F and 5G; Table S7).

As the primary function of FBXW7 is in protein degradation, we performed global cell proteomics to understand how this tumor suppressor and glutamine deprivation affect the proteome. Importantly, we found that PC was among the most significantly decreased proteins in *FBXW7*-depleted cells, independently of the presence of glutamine, and common to multiple cell lines (Figure 5H; Table S8; Figure S4). Neither *FBXW7* nor glutamine depletion affected the protein abundance of any other hits from our screen (Table S8). *PC* was one of the genes that scored highest among those dictating glutamine addiction (Figures 3B and 3C). Therefore, low PC expression is fully compatible with both the defects in pyruvate metabolism and the impaired growth observed in *FBXW7*-deficient cells in the absence of glutamine. To test for a causal role, we overexpressed a *PC* cDNA in *FBXW7*-depleted cells (Figure 5I). We found that *PC* overexpression not only conferred a growth advantage to cells during glutamine deprivation, but it also rescued the proliferation of *FBXW7*-depleted cells to the same extent as in control cells,

Please cite this article in press as: Lisci et al., Functional nutrient-genetic profiling reveals biotin and FBXW7 are essential to bypass glutamine addiction, Molecular Cell (2026), https://doi.org/10.1016/j.molcel.2026.02.002

CellPress
OPEN ACCESS

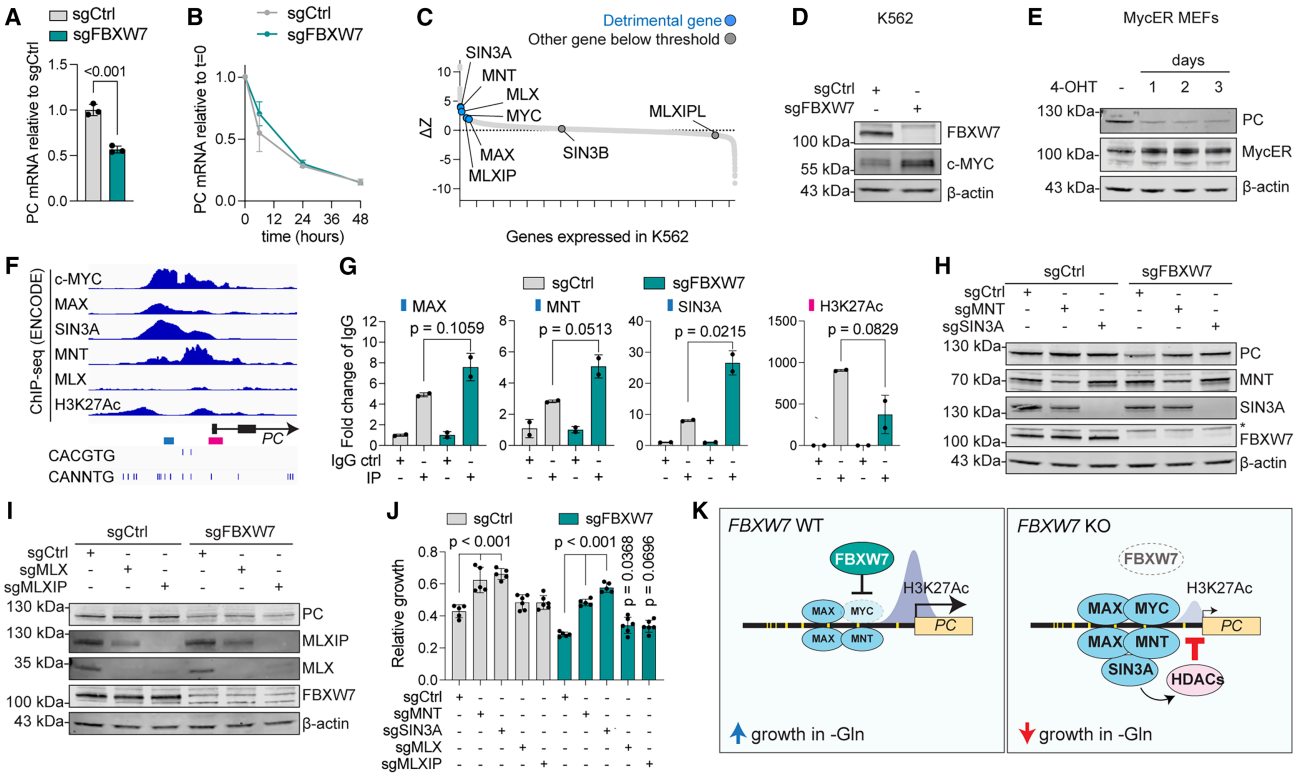

Figure 6. PC expression is repressed by c-MYC and MNT/SIN3A-dependent histone deacetylation

(A) PC mRNA expression in control (sgCtrl) and *FBXW7*-depleted (sgFBXW7) K562. *p* value, unpaired *t* test.

(B) PC mRNA decay in actinomycin-treated control and *FBXW7*-deficient K562.

(C) Gene essentiality score ($\Delta Z = Z_{-Gln} - Z_{+Gln}$) for transcriptional regulators in the MYC extended network. Blue dots, genes detrimental to the proliferation of glutamine-starved cells ($\Delta Z > 2$); gray dots, genes below threshold.

(D) c-MYC expression in control and *FBXW7*-depleted K562.

(E) c-MYC and PC expression in MycER mouse embryonic fibroblasts (MEFs) treated with 4-hydroxytamoxifen (4-OHT).

(F) ENCODE ChIP-seq data in K562 showing c-MYC, MAX, SIN3A, MNT, and MLX predicted binding sites and H3K27 acetylation (H3K27Ac) on the *PC* promoter. Regions amplified by ChIP-qPCR are labeled in blue (MAX, MNT, and SIN3A) and magenta (H3K27Ac). CACGTG and CANNTG, canonical and non-canonical E-boxes, respectively. Peaks are represented by setting the same data range (signal *p* value, 0–25) except for c-MYC (signal *p* value, 0–35).

(G) ChIP-qPCR in K562 for MAX, MNT, SIN3A, and H3K27Ac binding on the *PC* promoter. Vertical bars next to graph titles correspond to primer sets as shown in (F). *p* values, unpaired *t* tests.

(H and I) PC expression in *MNT* or *SIN3A*-depleted (H) and in *MLX* or *MLXIP*-depleted (I) sgCtrl and sgFBXW7 K562. * = non-specific band.

(J) Proliferation of control and *FBXW7*-deficient K562 depleted of *MNT*, *SIN3A*, *MLX*, or *MLXIP* and cultured in glutamine-deprived medium supplemented with pyruvate. Values represent the relative growth of each sample in comparison to proliferation in a glutamine-rich medium. *p* values, one-way ANOVA.

(K) Proposed model of *PC* transcriptional regulation by WT FBXW7, or upon FBXW7 depletion (KO). Yellow bars. E-boxes. Gln, glutamine. All data are represented as mean ± SD. Only *p* values < 0.05 are shown, except where indicated.

See also Figure S5.

suggesting an epistatic effect (Figure 5J). Taken together, our results indicate that *FBXW7* promotes proliferation in the absence of glutamine by supporting *PC* expression and subsequently pyruvate anaplerosis.

An FBXW7-MYC-MNT-SIN3A axis regulates PC expression via histone deacetylation

Our observation that PC protein abundance is reduced in the absence of *FBXW7* was unexpected given the role of FBXW7 in protein degradation and because these proteins are not localized in the same cellular compartment.[56–58] To investigate this further, we measured the transcript levels of *PC* and observed that they were significantly decreased in *FBXW7*-depleted cells (Figure 6A), mirroring reduced PC protein abundance (Figure 5I). PC mRNA stability was not affected (Figure 6B), suggesting FBXW7 modulates *PC* expression by regulating factors that affect its transcription.

We reasoned that genes involved in *PC* transcription might also affect proliferation in the absence of glutamine. Thus, we mined our genome-wide CRISPR-Cas9 screen and found a cluster of transcriptional regulators whose depletion was beneficial for growth in the absence of glutamine (Figures 6C and S5A). These included *MYC*, *MAX*, *MNT*, *SIN3A*, *MLX*, and *MLXIP*, known as the MYC extended network.[59] These factors bind to both canonical and non-canonical E-boxes to modulate

Please cite this article in press as: Lisci et al., Functional nutrient-genetic profiling reveals biotin and FBXW7 are essential to bypass glutamine addiction, Molecular Cell (2026), https://doi.org/10.1016/j.molcel.2026.02.002

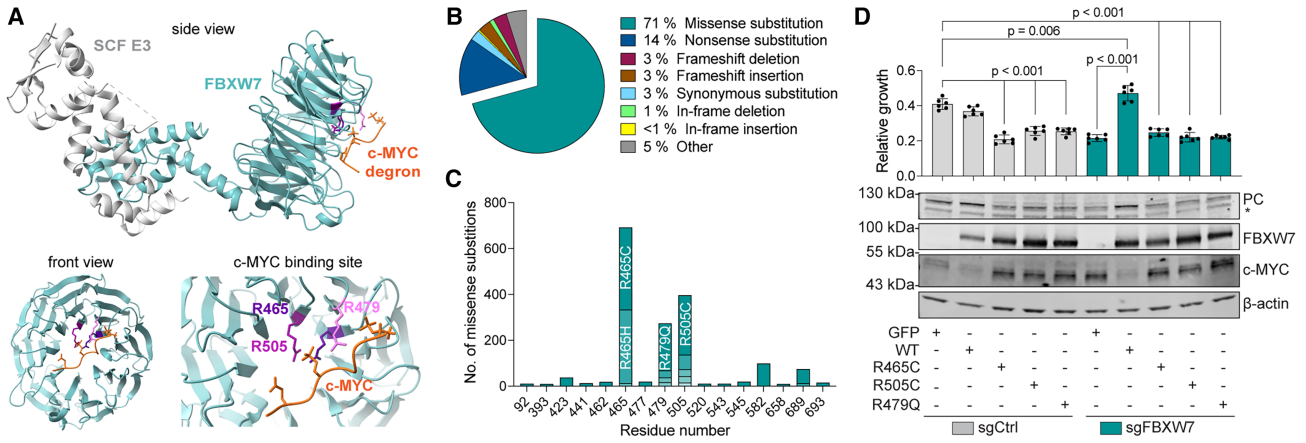

Figure 7. Cancer-associated mutations in FBXW7 lead to reduced PC expression and glutamine addiction

(A) Crystal structure of SCF E3 ubiquitin ligase (gray), FBXW7 (teal), and c-MYC degron (orange) (1.95 Å, PBD: 7D1Y). Most commonly mutated FBXW7 residues in cancer (R465, R505, and R479) are labeled in shades of purple. Top, side view. Bottom, front view (left) and magnification of c-MYC-binding site (right).

(B and C) Mutations in the *FBXW7* gene (B) and distribution of missense substitutions along the FBXW7 protein sequence (C). The four most common missense substitutions are highlighted (R465H, R465C, R479Q, and R505C) (source, COSMIC).

(D) Proliferation (top) and immunoblot (bottom) of control (sgCtrl) and *FBXW7*-depleted (sgFBXW7) K562 overexpressing WT FBXW7, cancer-associated FBXW7 mutations, or GFP control. Proliferation is shown in glutamine-deprived medium supplemented with pyruvate. Values represent the relative growth of each sample in comparison to proliferation in a glutamine-rich medium. * = non-specific band. All data are represented as mean ± SD. *p* values, one-way ANOVA. Only *p* values < 0.05 are shown.

transcription,[60] and they can form different heterodimers based on c-MYC accumulation.[61] Notably, MNT is known as a c-MYC antagonist[62] that competes with c-MYC for MAX binding. MNT recruits the transcriptional repressor SIN3A, which in turn recruits histone deacetylases, thus inhibiting gene expression.[63,64]

As c-MYC is a target of FBXW7, we first confirmed its accumulation in *FBXW7*-depleted K562 (Figure 6D). We then focused on the effects of its overexpression, rather than depletion, as *MYC* is in the top 1% of essential genes in K562.[65] To this aim, we employed the MycER mouse embryonic fibroblast line, in which tamoxifen addition initiates c-MYC translocation to the nucleus and DNA binding, a model that has been extensively used to study *MYC*, including in glutamine addiction.[9,18] Importantly, we found that *MYC* overexpression was sufficient to reduce PC protein abundance (Figure 6E), mirroring the results obtained in *FBXW7*-depleted K562 and supporting a repressive role for *MYC* on PC expression.

Next, we focused on the network of transcriptional inhibitors highlighted by our glutamine-sensitized screen. MNT and SIN3A can act as transcriptional repressors by binding genomic DNA and recruiting histone deacetylases (HDACs) to lysine 27 of histone 3 (H3K27).[63,64] We mined existing databases to probe for binding of these transcriptional repressors to the PC promoter, as well as for H3K27 acetylation (H3K27Ac), one of the main epigenetic alterations in cancers driven by *FBXW7* loss of function.[66] We first analyzed chromatin immunoprecipitation (ChIP) and sequencing data from the Encyclopedia of DNA Elements (ENCODE) project[67] in K562. We observed a clear signature for recruitment of c-MYC, MAX, MNT, and SIN3A on the *PC* promoter, as well as H3K27Ac peaks, all in the vicinity of E-boxes (Figure 6F). MLX showed no or little binding, and MLXIP ChIP-seq data were not available for K562. Notably, none of these factors changed in protein abundance following *FBXW7* or glutamine depletion (Table S8; Figure S5B). We next performed ChIP in control and *FBXW7*-deficient cells and measured binding of transcriptional modulators (MAX, MNT, and SIN3A) as well as H3K27Ac at the *PC* promoter. Importantly, we found that *FBXW7* depletion increased binding of MAX, MNT, and SIN3A to the *PC* promoter and reduced acetylation of the downstream H3K27 site (Figure 6G), suggesting a role for these transcriptional repressors in controlling *PC* expression.

To test this hypothesis, we used CRISPR-Cas9 to individually deplete *MNT*, *SIN3A*, *MLX*, and *MLXIP* in both control and *FBXW7*-deficient cells. Importantly, we observed that depletion of the transcriptional repressors *MNT* or *SIN3A* fully rescued both PC expression and proliferation in glutamine-deprived medium in an *FBXW7*-deficient background, indicating epistasis (Figures 6H and 6J). By contrast, *MLX* and *MLXIP*, which showed a less significant score in our screen (Figure 6C, Table S6), did not affect PC protein expression but provided a statistically significant yet minor rescue in glutamine-starved conditions (Figures 6I and 6J). Taken together, our data indicate that upon increased c-MYC expression in *FBXW7*-depleted cells, a cluster of transcriptional repressors recruits HDACs on the *PC* promoter, leading to decreased local H3K27 acetylation, lower *PC* expression, impaired pyruvate anaplerosis, and glutamine dependency (Figure 6K).

Engineered cancer-associated mutations in FBXW7 lead to glutamine addiction

Finally, we aimed to determine the clinical relevance of our model using cancer-associated *FBXW7* mutations. To this end, we mined protein structure (PDB: 7D1Y)[68] and cancer mutation (Catalogue of Somatic Mutations in Cancer, COSMIC)

databases and identified R465, R505, and R479 as the most frequently mutated residues in *FBXW7*-derived tumors.[69] These mutants are predominantly located in the substrate-binding pocket, affecting FBXW7-mediated recognition of target proteins, such as c-MYC (Figure 7A). Notably, the large majority of patient-associated FBXW7 mutations consist of missense substitutions altering the charge of residues in the substrate-binding pocket (R465H, R465C, R505C, and R479Q) (Figures 7B and 7C). To test whether these loss-of-function mutants would mimic the phenotypes we observed in *FBXW7*-depleted cells, we overexpressed WT and mutant *FBXW7* (R465C, R505C, and R479Q) in either an *FBXW7*-depleted or WT background. Strikingly, overexpression of all *FBXW7* mutants led to increased stabilization of c-MYC, reduced expression of PC, and inhibited proliferation in glutamine-deprived medium despite pyruvate supplementation (Figure 7D). These effects were apparent even in WT cells, mirroring the dominant negative effect of *FBXW7* mutations in patients[69] and linking them to glutamine addiction.

DISCUSSION

Here, we employed parallel nutrient and genetic screening to provide a comprehensive inventory of metabolites and molecular pathways required for proliferation in glutamine-deprived environments. Our systematic approach confirmed the results of previous work that identified metabolites that compensate for glutamine depletion, including carboxylic acids, aspartate, and asparagine.[15–17,24] In addition, we provide a direct comparison between hundreds of nutrients, covering most of the diversity found in plasma and in tumor interstitial fluid.[2,12] Our data highlight carbon-only molecules such as pyruvate and TCA cycle-related metabolites as the main determinants for cell proliferation in the absence of glutamine. While glutamine is both a carbon and a nitrogen source, previous and our findings indicate that its involvement in central carbon metabolism outweighs its role as a nitrogen donor,[5] possibly due to other nitrogen-containing molecules, such as amino acids, present in the environment. We confirmed the role of pyruvate in carbon metabolism using a ^{13}C-labeled tracer, showing significant incorporation of pyruvate-derived carbon into TCA cycle intermediates as well as in aspartate and asparagine. In agreement with earlier studies, we showed that aspartate or asparagine supplementation was sufficient to restore proliferation in glutamine-restricted cells.[16,17,24]

We built on the observation that pyruvate-supplemented cells could survive glutamine starvation to design a genome-wide CRISPR-Cas9 screen to identify genes involved in the proliferation of glutamine-restricted cells upon pyruvate supplementation. Integrating data from our nutrient and genetic screens, ^{13}C-pyruvate tracer, and earlier literature, we propose a unified model in which pyruvate licenses proliferation in glutamine-limiting conditions by serving as an anaplerotic substrate for PC, thus promoting mitochondrial aspartate biogenesis as well as export to the cytosol via the MAS, contributing to asparagine, protein, and nucleotide synthesis. In support of this model, we showed that depleting the mitochondrial arm of the MAS (aspartate export) is detrimental in glutamine-limited conditions, while depleting its cytosolic arm (aspartate import into mitochondria) is beneficial. We also report that in glutamine-deprived cells the amino acid deprivation-sensing arm of the ISR is required for survival, while its downstream effector *SLC7A11* and its binding partner *SLC3A2* are detrimental. As these proteins form the plasma membrane cystine/glutamate exchanger system X_c^-, this could be explained by conservation of intracellular glutamate. Our findings are supported by previous work[36] and warrant caution in the use of the system X_c^- inhibitors currently being developed for cancer therapy, as they could promote cell survival in a glutamine-limited tumor microenvironment. Importantly, our results also highlight the need for the vitamin biotin and for biotin import and conjugation to proteins, providing an essential cofactor for PC. Together, our findings extend previous work and provide a comprehensive resource identifying both the metabolites and the genes modulating survival of glutamine-starved cells.

Our analysis highlighted the tumor suppressor gene *FBXW7* as a central regulator of pyruvate metabolism. *FBXW7* is one of the most highly mutated genes in cancers[70,71] and degrades the protein product of several proto-oncogenes, including c-MYC, c-JUN, and cyclin E.[52–55] *FBXW7* also influences epigenetic remodeling via H3K27 acetylation and tri-methylation and by acting upstream of c-MYC.[66] While *FBXW7* has been linked to oxidative and liver metabolism,[72,73] the mechanism behind these observations remains unclear. We report that *FBXW7* mediates anaplerosis by promoting the expression of *PC*. *FBXW7* depletion reduces proliferation in glutamine-deprived environments, independently of pyruvate supplementation. This leads to decreased carbon flux by inhibiting pyruvate utilization in the TCA cycle, limiting aspartate and asparagine synthesis. We highlight PC as the limiting factor for the metabolic flexibility of *FBXW7*-deficient cells, thus leading to glutamine addiction.

We confirmed c-MYC accumulation upon *FBXW7* depletion and report that c-MYC upregulation is sufficient to inhibit *PC* expression in WT cells. While c-MYC is classically viewed as a transcriptional promoter, its modulation of gene expression is achieved in concert with a network of transcriptional regulators known as the MYC extended network (Figure S5A).[59] This includes the c-MYC-binding partner MAX, as well as MNT, MLX, and MLXIP. These proteins form heterodimers that bind E-boxes, either cooperating with or competing against c-MYC-dependent transcription.[59] While MLX/MLXIP were suggested to affect c-MYC-dependent metabolic pathways,[74] the role of MNT in metabolism remains to be explored. By competing for MAX, MNT acts as a c-MYC antagonist[61,62] and inhibits gene expression by recruiting the transcriptional repressor SIN3A and subsequently histone deacetylases.[63,64] c-MYC/MAX and MNT/MAX heterodimers can co-exist in cells, but MNT-mediated repression can be dominant over c-MYC transcriptional activation.[61,75] We mined the ENCODE database and showed that c-MYC, MAX, MNT, and SIN3A bind the *PC* promoter upstream of an H3K27 acetylation peak. The *PC* promoter is characterized by the presence of multiple E-boxes, suggesting complex binding by the MYC extended network. We show that *FBXW7* depletion increases recruitment of MAX, MNT, and SIN3A to the *PC* promoter and decreases H3K27 acetylation. This inhibits *PC* expression, consistent with a dominant role for

MNT/MAX heterodimers in transcriptional repression despite c-MYC accumulation in *FBXW7*-deficient cells.

c-MYC is a known driver of glutamine addiction that promotes expression of glutaminase and glutamine transporters.[8–11,22] Despite c-MYC accumulation and glutamine dependency of K562, our proteomics analysis of *FBXW7*-depleted cells did not identify altered expression of these glutamine-related genes, suggesting cell-specific differences. Rather, we observed reduced PC levels across seven *FBXW7*-depleted human cell lines and showed that *PC* overexpression restores growth of *FBXW7*-deficient cells, indicating that *PC* is both necessary and sufficient to promote proliferation upon glutamine depletion. Our findings provide a better understanding of metabolic pathways regulated by *FBXW7* and identify PC as the main downstream effector of FBXW7/c-MYC in glutamine addiction. Interestingly, while some hotspot mutations in *FBXW7* share a similar distribution pattern across affected tissues, others appear to be tissue-specific[69] and could reflect the ability of *FBXW7* mutations to impair substrate binding and inhibit proliferation in glutamine-limited environments. Furthermore, our results suggest that c-MYC upregulation is sufficient to decrease *PC* expression even in WT cells, highlighting pyruvate carboxylation as a metabolic vulnerability to be targeted for cancer therapy.

An interesting aspect of our findings is the decrease in *PC* expression, and thus glutamine addiction, in cells overexpressing MYC. We propose two physiological conditions in which this mechanism could be relevant for proliferation. First, *MYC* coordinates metabolic reprogramming during physiological processes such as pluripotent stem cell differentiation[76,77] and hematopoiesis.[78] *PC* repression could limit the role of pyruvate in anaplerosis to promote its use in redox balance via conversion to lactate, thereby enforcing a glycolytic, biomass-producing state that relies on glutamine to replenish the TCA cycle. Secondly, the dependence on glutamine may act as an intrinsic nutrient checkpoint: *MYC*-driven proliferation proceeds efficiently only when key nutrients, including glutamine, are abundant, providing a built-in safeguard mechanism that would halt uncontrolled cell proliferation in an environment unable to sustain it. Notably, pyruvate import via the mitochondrial pyruvate carrier plays a role in cell differentiation.[79,80] We speculate that altering the carbon entry point into the TCA cycle by modulating PC and PDH activity could be a regulatory node in cells with high *MYC* expression to modulate differentiation and proliferation.

Altogether, our study highlights the power of nutrient-based screening coupled with genetic perturbation strategies to provide a better understanding of the metabolic flexibility of mammalian cells facing nutrient deprivation. We provide a unified model of the molecular mechanisms of glutamine addiction, an important resource for further investigations in the field. Nutrient fluctuations, including glutamine scarcity, can challenge the growth of mammalian cells in different physiological states, such as tissue migration, cell growth, and differentiation. Investigating how cells cope with such heterogeneous conditions will increase our knowledge of the factors supporting metabolic flexibility and could provide applications in pathological settings, deepening our understanding of how cancer initiation and progression can be shaped by glutamine addiction.

Limitations of the study

We systematically analyzed nutrients and molecular pathways modulating the proliferation of glutamine-restricted cells. A common limitation of genetic screens performed in a pooled format is cross-feeding (nutrient transfer between cells via the culture medium) and competition between cells in the population. While we validated many of our hits, future work should include continuing the experimental validation of genes and metabolites highlighted in our screens. Moreover, as we targeted one gene at a time in our assays, it remains possible that compensatory mechanisms and gene redundancy might have masked the involvement of some genes in glutamine-related pathways.

We validated our results in several human and murine cancer cell lines grown in two or three dimensions, as well as in primary cells. In the future, it will be important to further validate our findings in cancer models. We also assigned a role for *FBXW7* in *PC* regulation and pyruvate metabolism: while we focused on the MYC extended network, including MNT and SIN3A, both FBXW7 and c-MYC have a wide range of targets. We do not exclude that additional layers of regulation may exist downstream of *FBXW7* and upstream of *PC* that could contribute to pyruvate anaplerosis and cell proliferation in glutamine-deprived conditions.

RESOURCE AVAILABILITY

Lead contact

Requests for further information and resources should be directed to and will be fulfilled by the lead contact, Alexis Jourdain (alexis.jourdain@unil.ch).

Materials availability

All unique/stable reagents generated in this study are available from the lead contact with a completed materials transfer agreement.

Data and code availability

- All metabolomics and mass spectrometry data have been deposited as follows: ^{13}C- and ^{15}N-glutamine isotopic profiling data at MetaboLights: MTBLS13799; multiple pathway targeted analysis of polar metabolites datasets at Zenodo: 14002048; ^{13}C-pyruvate isotopic profiling data in K562 at Zenodo: 14002048; ^{13}C-pyruvate isotopic profiling data in T cells at MetaboLights: MTBLS13799; mass spectrometry data at ProteomeXchange Consortium via the PRIDE partner repository: PXD057389; raw spheroid imaging data at Mendeley Data: https://www.doi.org/10.17632/328g7zyt9d.1). All deposited data are publicly available as of the date of publication.
- This paper does not report original code.
- Any additional information required to reanalyze the data reported in this paper is available from the lead contact upon request.

ACKNOWLEDGMENTS

The authors would like to thank past and present members of the Jourdain laboratory, M. Knobloch, F. Langlet, J.C. Martinou, K. Maundrell, A. Mayer, L. Mazzeo, M. Quadroni, the Metabolomics Platform and the Protein Analysis Facility (University of Lausanne), and the Genome Perturbation Platform (Broad Institute). MycER mouse embryonic fibroblasts were a gift from R. Mostoslavsky (Harvard Medical School). This project was supported by an EMBO postdoctoral fellowship (ALTF286-2022 to M.L.), the EMBO Young Investigator Programme (to A.A.J.), and the Swiss National Science Foundation (310030_200796 and 3200-0-239867 to A.A.J.).

AUTHOR CONTRIBUTIONS

M.L.: investigation (lead), methodology (equal), validation (lead), data curation (lead), project administration (equal), formal analysis (lead), visualization, funding acquisition (supporting), and writing (original draft preparation, equal). F.V.: investigation (supporting), data curation (supporting), and writing (reviewing and editing, equal). Y.L.: methodology (supporting), data curation (supporting), formal analysis (supporting), and writing (reviewing and editing, equal). H.G.-A.: formal analysis (supporting) and data curation (supporting). J.I.: methodology (equal), formal analysis (supporting), data curation (supporting), and writing (reviewing and editing, equal). O.S.S.: investigation (supporting), methodology (supporting), data curation (supporting), formal analysis (supporting), and writing (reviewing and editing, equal). A.A.J.: conceptualization, methodology (equal), project administration (equal), supervision (lead), funding acquisition (lead), and writing (original draft preparation, equal).

DECLARATION OF INTERESTS

A.A.J. is listed as an inventor on a patent related to system X_c^- inhibition. O.S.S. previously served as a consultant for Handshake AI.

DECLARATION OF GENERATIVE AI AND AI-ASSISTED TECHNOLOGIES

No generative AI or AI-assisted technology was employed for conceptualization or investigation in the course of this project.

STAR★METHODS

Detailed methods are provided in the online version of this paper and include the following:

- KEY RESOURCES TABLE
- EXPERIMENTAL MODEL AND STUDY PARTICIPANT DETAILS
  - Cell lines
  - Primary cells
- METHOD DETAILS
  - Spheroid culture
  - Proliferation assays
  - Cloning and lentiviral infection
  - Genome-wide CRISPR-Cas9 screen
  - BioLog nutrient screen
  - Immunoblotting
  - RNA extraction, cDNA synthesis and qPCR
  - Chromatin immunoprecipitation (ChIP)-qPCR
  - Protein mass spectrometry
  - Multiple pathway metabolomics analysis of polar metabolites
  - NADH and NAD^+ quantification
  - ^{13}C-pyruvate isotopic profiling
  - ^{13}C-glutamine and ^{15}N-glutamine isotopic profiling
- QUANTIFICATION AND STATISTICAL ANALYSIS

SUPPLEMENTAL INFORMATION

Supplemental information can be found online at https://doi.org/10.1016/j.molcel.2026.02.002.

Received: November 12, 2024
Revised: December 9, 2025
Accepted: February 2, 2026

REFERENCES

1. Smith, R.L., Soeters, M.R., Wüst, R.C.I., and Houtkooper, R.H. (2018). Metabolic Flexibility as an Adaptation to Energy Resources and Requirements in Health and Disease. Endocr. Rev. *39*, 489–517. https://doi.org/10.1210/er.2017-00211.
2. Wishart, D.S., Guo, A., Oler, E., Wang, F., Anjum, A., Peters, H., Dizon, R., Sayeeda, Z., Tian, S., Lee, B.L., et al. (2022). HMDB 5.0: the Human Metabolome Database for 2022. Nucleic Acids Res. *50*, D622–D631. https://doi.org/10.1093/nar/gkab1062.
3. McMenamy, R.H., Lund, C.C., and Oncley, J.L. (1957). Unbound amino acid concentrations in human blood plasmas. J. Clin. Investig. *36*, 1672–1679. https://doi.org/10.1172/JCI103568.
4. Eagle, H., Oyama, V.I., Levy, M., Horton, C.L., and Fleischman, R. (1956). The growth response of mammalian cells in tissue culture to L-glutamine and L-glutamic acid. J. Biol. Chem. *218*, 607–616. https://doi.org/10.1016/S0021-9258(18)65826-0.
5. DeBerardinis, R.J., Mancuso, A., Daikhin, E., Nissim, I., Yudkoff, M., Wehrli, S., and Thompson, C.B. (2007). Beyond aerobic glycolysis: transformed cells can engage in glutamine metabolism that exceeds the requirement for protein and nucleotide synthesis. Proc. Natl. Acad. Sci. USA *104*, 19345–19350. https://doi.org/10.1073/pnas.0709747104.
6. Zhang, J., Pavlova, N.N., and Thompson, C.B. (2017). Cancer cell metabolism: the essential role of the nonessential amino acid, glutamine. EMBO J. *36*, 1302–1315. https://doi.org/10.15252/embj.201696151.
7. Pavlova, N.N., Zhu, J., and Thompson, C.B. (2022). The hallmarks of cancer metabolism: Still emerging. Cell Metab. *34*, 355–377. https://doi.org/10.1016/j.cmet.2022.01.007.
8. Bott, A.J., Peng, I.C., Fan, Y., Faubert, B., Zhao, L., Li, J., Neidler, S., Sun, Y., Jaber, N., Krokowski, D., et al. (2015). Oncogenic Myc Induces Expression of Glutamine Synthetase through Promoter Demethylation. Cell Metab. *22*, 1068–1077. https://doi.org/10.1016/j.cmet.2015.09.025.
9. Wise, D.R., DeBerardinis, R.J., Mancuso, A., Sayed, N., Zhang, X.Y., Pfeiffer, H.K., Nissim, I., Daikhin, E., Yudkoff, M., McMahon, S.B., et al. (2008). Myc regulates a transcriptional program that stimulates mitochondrial glutaminolysis and leads to glutamine addiction. Proc. Natl. Acad. Sci. USA *105*, 18782–18787. https://doi.org/10.1073/pnas.0810199105.
10. Zhao, X., Petrashen, A.P., Sanders, J.A., Peterson, A.L., and Sedivy, J.M. (2019). SLC1A5 glutamine transporter is a target of MYC and mediates reduced mTORC1 signaling and increased fatty acid oxidation in long-lived Myc hypomorphic mice. Aging Cell *18*, e12947. https://doi.org/10.1111/acel.12947.
11. Yuneva, M., Zamboni, N., Oefner, P., Sachidanandam, R., and Lazebnik, Y. (2007). Deficiency in glutamine but not glucose induces MYC-dependent apoptosis in human cells. J. Cell Biol. *178*, 93–105. https://doi.org/10.1083/jcb.200703099.
12. Sullivan, M.R., Danai, L.V., Lewis, C.A., Chan, S.H., Gui, D.Y., Kunchok, T., Dennstedt, E.A., Vander Heiden, M.G., and Muir, A. (2019). Quantification of microenvironmental metabolites in murine cancers reveals determinants of tumor nutrient availability. eLife *8*, e44235. https://doi.org/10.7554/eLife.44235.
13. Edwards, D.N., Ngwa, V.M., Raybuck, A.L., Wang, S., Hwang, Y., Kim, L.C., Cho, S.H., Paik, Y., Wang, Q., Zhang, S., et al. (2021). Selective glutamine metabolism inhibition in tumor cells improves antitumor T lymphocyte activity in triple-negative breast cancer. J. Clin. Investig. *131*, e140100. https://doi.org/10.1172/JCI140100.
14. Reinfeld, B.I., Madden, M.Z., Wolf, M.M., Chytil, A., Bader, J.E., Patterson, A.R., Sugiura, A., Cohen, A.S., Ali, A., Do, B.T., et al. (2021). Cell-programmed nutrient partitioning in the tumour microenvironment. Nature *593*, 282–288. https://doi.org/10.1038/s41586-021-03442-1.
15. Cheng, T., Sudderth, J., Yang, C., Mullen, A.R., Jin, E.S., Matés, J.M., and DeBerardinis, R.J. (2011). Pyruvate carboxylase is required for glutamine-independent growth of tumor cells. Proc. Natl. Acad. Sci. USA *108*, 8674–8679. https://doi.org/10.1073/pnas.1016627108.
16. Pavlova, N.N., Hui, S., Ghergurovich, J.M., Fan, J., Intlekofer, A.M., White, R.M., Rabinowitz, J.D., Thompson, C.B., and Zhang, J. (2018).

As Extracellular Glutamine Levels Decline, Asparagine Becomes an Essential Amino Acid. Cell Metab. *27*, 428–438.e5. https://doi.org/10.1016/j.cmet.2017.12.006.

17. Zhang, J., Fan, J., Venneti, S., Cross, J.R., Takagi, T., Bhinder, B., Djaballah, H., Kanai, M., Cheng, E.H., Judkins, A.R., et al. (2014). Asparagine plays a critical role in regulating cellular adaptation to glutamine depletion. Mol. Cell *56*, 205–218. https://doi.org/10.1016/j.molcel.2014.08.018.
18. Linder, S.J., Bernasocchi, T., Martínez-Pastor, B., Sullivan, K.D., Galbraith, M.D., Lewis, C.A., Ferrer, C.M., Boon, R., Silveira, G.G., Cho, H.M., et al. (2023). Inhibition of the proline metabolism rate-limiting enzyme P5CS allows proliferation of glutamine-restricted cancer cells. Nat. Metab. *5*, 2131–2147. https://doi.org/10.1038/s42255-023-00919-3.
19. UniProt Consortium (2025). UniProt: the universal protein knowledgebase in 2025. Nucleic Acids Res. *53*, D609–D617. https://doi.org/10.1093/nar/gkae1010.
20. Altman, B.J., Stine, Z.E., and Dang, C.V. (2016). From Krebs to clinic: glutamine metabolism to cancer therapy. Nat. Rev. Cancer *16*, 619–634. https://doi.org/10.1038/nrc.2016.71.
21. Moreadith, R.W., and Lehninger, A.L. (1984). The pathways of glutamate and glutamine oxidation by tumor cell mitochondria. Role of mitochondrial NAD(P)+-dependent malic enzyme. J. Biol. Chem. *259*, 6215–6221. https://doi.org/10.1016/S0021-9258(20)82128-0.
22. Le, A., Lane, A.N., Hamaker, M., Bose, S., Gouw, A., Barbi, J., Tsukamoto, T., Rojas, C.J., Slusher, B.S., Zhang, H., et al. (2012). Glucose-independent glutamine metabolism via TCA cycling for proliferation and survival in B cells. Cell Metab. *15*, 110–121. https://doi.org/10.1016/j.cmet.2011.12.009.
23. Cantor, J.R., Abu-Remaileh, M., Kanarek, N., Freinkman, E., Gao, X., Louissaint, A., Jr., Lewis, C.A., and Sabatini, D.M. (2017). Physiologic Medium Rewires Cellular Metabolism and Reveals Uric Acid as an Endogenous Inhibitor of UMP Synthase. Cell *169*, 258–272.e17. https://doi.org/10.1016/j.cell.2017.03.023.
24. Alkan, H.F., Walter, K.E., Luengo, A., Madreiter-Sokolowski, C.T., Stryeck, S., Lau, A.N., Al-Zoughbi, W., Lewis, C.A., Thomas, C.J., Hoefler, G., et al. (2018). Cytosolic Aspartate Availability Determines Cell Survival When Glutamine Is Limiting. Cell Metab. *28*, 706–720.e6. https://doi.org/10.1016/j.cmet.2018.07.021.
25. Sullivan, L.B., Gui, D.Y., Hosios, A.M., Bush, L.N., Freinkman, E., and Vander Heiden, M.G. (2015). Supporting Aspartate Biosynthesis Is an Essential Function of Respiration in Proliferating Cells. Cell *162*, 552–563. https://doi.org/10.1016/j.cell.2015.07.017.
26. To, T.L., Cuadros, A.M., Shah, H., Hung, W.H.W., Li, Y., Kim, S.H., Rubin, D.H.F., Boe, R.H., Rath, S., Eaton, J.K., et al. (2019). A Compendium of Genetic Modifiers of Mitochondrial Dysfunction Reveals Intra-organelle Buffering. Cell *179*, 1222–1238.e17. https://doi.org/10.1016/j.cell.2019.10.032.
27. Karmen, A., Wroblewski, F., and Ladue, J.S. (1955). Transaminase activity in human blood. J. Clin. Investig. *34*, 126–131. https://doi.org/10.1172/JCI103055.
28. Pang, Z., Lu, Y., Zhou, G., Hui, F., Xu, L., Viau, C., Spigelman, A.F., MacDonald, P.E., Wishart, D.S., Li, S., et al. (2024). MetaboAnalyst 6.0: towards a unified platform for metabolomics data processing, analysis and interpretation. Nucleic Acids Res. *52*, W398–W406. https://doi.org/10.1093/nar/gkae253.
29. Birsoy, K., Wang, T., Chen, W.W., Freinkman, E., Abu-Remaileh, M., and Sabatini, D.M. (2015). An Essential Role of the Mitochondrial Electron Transport Chain in Cell Proliferation Is to Enable Aspartate Synthesis. Cell *162*, 540–551. https://doi.org/10.1016/j.cell.2015.07.016.
30. Titov, D.V., Cracan, V., Goodman, R.P., Peng, J., Grabarek, Z., and Mootha, V.K. (2016). Complementation of mitochondrial electron transport chain by manipulation of the NAD^+/NADH ratio. Science *352*, 231–235. https://doi.org/10.1126/science.aad4017.
31. Tanaka, K., Sasayama, T., Nagashima, H., Irino, Y., Takahashi, M., Izumi, Y., Uno, T., Satoh, N., Kitta, A., Kyotani, K., et al. (2021). Glioma cells require one-carbon metabolism to survive glutamine starvation. Acta Neuropathol. Commun. *9*, 16. https://doi.org/10.1186/s40478-020-01114-1.
32. Tajan, M., Hock, A.K., Blagih, J., Robertson, N.A., Labuschagne, C.F., Kruiswijk, F., Humpton, T.J., Adams, P.D., and Vousden, K.H. (2018). A Role for p53 in the Adaptation to Glutamine Starvation through the Expression of SLC1A3. Cell Metab. *28*, 721–736.e6. https://doi.org/10.1016/j.cmet.2018.07.005.
33. Sellers, K., Fox, M.P., Bousamra, M., 2nd, Slone, S.P., Higashi, R.M., Miller, D.M., Wang, Y., Yan, J., Yuneva, M.O., Deshpande, R., et al. (2015). Pyruvate carboxylase is critical for non-small-cell lung cancer proliferation. J. Clin. Investig. *125*, 687–698. https://doi.org/10.1172/JCI72873.
34. Pakos-Zebrucka, K., Koryga, I., Mnich, K., Ljujic, M., Samali, A., and Gorman, A.M. (2016). The integrated stress response. EMBO Rep. *17*, 1374–1395. https://doi.org/10.15252/embr.201642195.
35. Shin, C.S., Mishra, P., Watrous, J.D., Carelli, V., D'Aurelio, M., Jain, M., and Chan, D.C. (2017). The glutamate/cystine xCT antiporter antagonizes glutamine metabolism and reduces nutrient flexibility. Nat. Commun. *8*, 15074. https://doi.org/10.1038/ncomms15074.
36. Muir, A., Danai, L.V., Gui, D.Y., Waingarten, C.Y., Lewis, C.A., and Vander Heiden, M.G. (2017). Environmental cystine drives glutamine anaplerosis and sensitizes cancer cells to glutaminase inhibition. eLife *6*, e27713. https://doi.org/10.7554/eLife.27713.
37. Ye, P., Mimura, J., Okada, T., Sato, H., Liu, T., Maruyama, A., Ohyama, C., and Itoh, K. (2014). Nrf2- and ATF4-dependent upregulation of xCT modulates the sensitivity of T24 bladder carcinoma cells to proteasome inhibition. Mol. Cell. Biol. *34*, 3421–3434. https://doi.org/10.1128/MCB.00221-14.
38. Prasad, P.D., Wang, H., Huang, W., Fei, Y.J., Leibach, F.H., Devoe, L.D., and Ganapathy, V. (1999). Molecular and functional characterization of the intestinal Na+-dependent multivitamin transporter. Arch. Biochem. Biophys. *366*, 95–106. https://doi.org/10.1006/abbi.1999.1213.
39. Wang, H., Huang, W., Fei, Y.J., Xia, H., Yang-Feng, T.L., Leibach, F.H., Devoe, L.D., Ganapathy, V., and Prasad, P.D. (1999). Human placental Na+-dependent multivitamin transporter. Cloning, functional expression, gene structure, and chromosomal localization. J. Biol. Chem. *274*, 14875–14883. https://doi.org/10.1074/jbc.274.21.14875.
40. Suzuki, Y., Aoki, Y., Ishida, Y., Chiba, Y., Iwamatsu, A., Kishino, T., Niikawa, N., Matsubara, Y., and Narisawa, K. (1994). Isolation and characterization of mutations in the human holocarboxylase synthetase cDNA. Nat. Genet. *8*, 122–128. https://doi.org/10.1038/ng1094-122.
41. León-Del-Rio, A., Leclerc, D., Akerman, B., Wakamatsu, N., and Gravel, R.A. (1995). Isolation of a cDNA encoding human holocarboxylase synthetase by functional complementation of a biotin auxotroph of Escherichia coli. Proc. Natl. Acad. Sci. USA *92*, 4626–4630. https://doi.org/10.1073/pnas.92.10.4626.
42. Gao, J., Schatton, D., Martinelli, P., Hansen, H., Pla-Martin, D., Barth, E., Becker, C., Altmueller, J., Frommolt, P., Sardiello, M., et al. (2014). CLUH regulates mitochondrial biogenesis by binding mRNAs of nuclear-encoded mitochondrial proteins. J. Cell Biol. *207*, 213–223. https://doi.org/10.1083/jcb.201403129.
43. Lampert, F., Stafa, D., Goga, A., Soste, M.V., Gilberto, S., Olieric, N., Picotti, P., Stoffel, M., and Peter, M. (2018). The multi-subunit GID/CTLH E3 ubiquitin ligase promotes cell proliferation and targets the transcription factor Hbp1 for degradation. eLife *7*, e35528. https://doi.org/10.7554/eLife.35528.
44. Kobayashi, N., Yang, J., Ueda, A., Suzuki, T., Tomaru, K., Takeno, M., Okuda, K., and Ishigatsubo, Y. (2007). RanBPM, Muskelin, p48EMLP, p44CTLH, and the armadillo-repeat proteins ARMC8alpha and ARMC8beta are components of the CTLH complex. Gene *396*, 236–247. https://doi.org/10.1016/j.gene.2007.02.032.

45. Winston, J.T., Koepp, D.M., Zhu, C., Elledge, S.J., and Harper, J.W. (1999). A family of mammalian F-box proteins. Curr. Biol. *9*, 1180–1182. https://doi.org/10.1016/S0960-9822(00)80021-4.

46. Owens, D.D.G., Maitland, M.E.R., Khalili Yazdi, A., Song, X., Reber, V., Schwalm, M.P., Machado, R.A.C., Bauer, N., Wang, X., Szewczyk, M.M., et al. (2024). A chemical probe to modulate human GID4 Pro/N-degron interactions. Nat. Chem. Biol. *20*, 1164–1175. https://doi.org/10.1038/s41589-024-01618-0.

47. Kremer, D.M., Nelson, B.S., Lin, L., Yarosz, E.L., Halbrook, C.J., Kerk, S.A., Sajjakulnukit, P., Myers, A., Thurston, G., Hou, S.W., et al. (2021). GOT1 inhibition promotes pancreatic cancer cell death by ferroptosis. Nat. Commun. *12*, 4860. https://doi.org/10.1038/s41467-021-24859-2.

48. Son, J., Lyssiotis, C.A., Ying, H., Wang, X., Hua, S., Ligorio, M., Perera, R.M., Ferrone, C.R., Mullarky, E., Shyh-Chang, N., et al. (2013). Glutamine supports pancreatic cancer growth through a KRAS-regulated metabolic pathway. Nature *496*, 101–105. https://doi.org/10.1038/nature12040.

49. Lou, Y., Lou, Y., Cheng, Y., Xu, B., Chen, H., and Dai, Y. (2025). Panoramic view of MDH1: driving cancer progression and shaping the tumor immune microenvironment. Front. Immunol. *16*, 1631449. https://doi.org/10.3389/fimmu.2025.1631449.

50. Peng, H., Dou, H., He, S., Xie, Y.A., Zhang, Q., and Zheng, J. (2024). The role of GOT1 in cancer metabolism. Front. Oncol. *14*, 1519046. https://doi.org/10.3389/fonc.2024.1519046.

51. Zhou, F.Z., Zhang, Y., Zhu, Y., Zhou, Q., Shi, Y., and Hu, Q. (2024). Structural insights into human propionyl-CoA carboxylase (PCC) and 3-methylcrotonyl-CoA carboxylase (MCC). eLife *13*. https://doi.org/10.7554/eLife.98885.2.

52. Yada, M., Hatakeyama, S., Kamura, T., Nishiyama, M., Tsunematsu, R., Imaki, H., Ishida, N., Okumura, F., Nakayama, K., and Nakayama, K.I. (2004). Phosphorylation-dependent degradation of c-Myc is mediated by the F-box protein Fbw7. EMBO J. *23*, 2116–2125. https://doi.org/10.1038/sj.emboj.7600217.

53. Koepp, D.M., Schaefer, L.K., Ye, X., Keyomarsi, K., Chu, C., Harper, J.W., and Elledge, S.J. (2001). Phosphorylation-dependent ubiquitination of cyclin E by the SCFFbw7 ubiquitin ligase. Science *294*, 173–177. https://doi.org/10.1126/science.1065203.

54. Qi, Y., Rezaeian, A.H., Wang, J., Huang, D., Chen, H., Inuzuka, H., and Wei, W. (2024). Molecular insights and clinical implications for the tumor suppressor role of SCFFBXW7 E3 ubiquitin ligase. Biochim. Biophys. Acta Rev. Cancer *1879*, 189140. https://doi.org/10.1016/j.bbcan.2024.189140.

55. Wei, W., Jin, J., Schlisio, S., Harper, J.W., and Kaelin, W.G., Jr. (2005). The v-Jun point mutation allows c-Jun to escape GSK3-dependent recognition and destruction by the Fbw7 ubiquitin ligase. Cancer Cell *8*, 25–33. https://doi.org/10.1016/j.ccr.2005.06.005.

56. Welcker, M., Orian, A., Grim, J.E., Eisenman, R.N., and Clurman, B.E. (2004). A nucleolar isoform of the Fbw7 ubiquitin ligase regulates c-Myc and cell size. Curr. Biol. *14*, 1852–1857. https://doi.org/10.1016/j.cub.2004.09.083.

57. Matsumoto, A., Tateishi, Y., Onoyama, I., Okita, Y., Nakayama, K., and Nakayama, K.I. (2011). Fbxw7beta resides in the endoplasmic reticulum membrane and protects cells from oxidative stress. Cancer Sci. *102*, 749–755. https://doi.org/10.1111/j.1349-7006.2011.01851.x.

58. Utter, M.F., and Keech, D.B. (1960). Formation of oxaloacetate from pyruvate and carbon dioxide. J. Biol. Chem. *235*, PC17–PC18. https://doi.org/10.1016/S0021-9258(18)69442-6.

59. Conacci-Sorrell, M., McFerrin, L., and Eisenman, R.N. (2014). An overview of MYC and its interactome. Cold Spring Harb. Perspect. Med. *4*, a014357. https://doi.org/10.1101/cshperspect.a014357.

60. Liaño-Pons, J., Arsenian-Henriksson, M., and León, J. (2021). The Multiple Faces of MNT and Its Role as a MYC Modulator. Cancers (Basel) *13*, 4682. https://doi.org/10.3390/cancers13184682.

61. Hurlin, P.J., Quéva, C., and Eisenman, R.N. (1997). Mnt, a novel Max-interacting protein is coexpressed with Myc in proliferating cells and mediates repression at Myc binding sites. Genes Dev. *11*, 44–58. https://doi.org/10.1101/gad.11.1.44.

62. Yang, G., and Hurlin, P.J. (2017). MNT and Emerging Concepts of MNT-MYC Antagonism. Genes (Basel) *8*, 83. https://doi.org/10.3390/genes8020083.

63. Saunders, A., Huang, X., Fidalgo, M., Reimer, M.H., Jr., Faiola, F., Ding, J., Sánchez-Priego, C., Guallar, D., Sáenz, C., Li, D., et al. (2017). The SIN3A/HDAC Corepressor Complex Functionally Cooperates with NANOG to Promote Pluripotency. Cell Rep. *18*, 1713–1726. https://doi.org/10.1016/j.celrep.2017.01.055.

64. Lavin, D.P., Abassi, L., Inayatullah, M., and Tiwari, V.K. (2021). Mnt Represses Epithelial Identity To Promote Epithelial-to-Mesenchymal Transition. Mol. Cell. Biol. *41*, e0018321. https://doi.org/10.1128/MCB.00183-21.

65. Tsherniak, A., Vazquez, F., Montgomery, P.G., Weir, B.A., Kryukov, G., Cowley, G.S., Gill, S., Harrington, W.F., Pantel, S., Krill-Burger, J.M., et al. (2017). Defining a Cancer Dependency Map. Cell *170*, 564–576.e16. https://doi.org/10.1016/j.cell.2017.06.010.

66. Thirimanne, H.N., Wu, F., Janssens, D.H., Swanger, J., Diab, A., Feldman, H.M., Amezquita, R.A., Gottardo, R., Paddison, P.J., Henikoff, S., et al. (2022). Global and context-specific transcriptional consequences of oncogenic Fbw7 mutations. eLife *11*, e74338. https://doi.org/10.7554/eLife.74338.

67. Zhang, J., Lee, D., Dhiman, V., Jiang, P., Xu, J., McGillivray, P., Yang, H., Liu, J., Meyerson, W., Clarke, D., et al. (2020). An integrative ENCODE resource for cancer genomics. Nat. Commun. *11*, 3696. https://doi.org/10.1038/s41467-020-14743-w.

68. Huang, K.F., Huang, J.S., Wu, M.L., Hsieh, W.L., Hsu, K.C., Hsu, H.L., Ko, T.P., and Wang, A.H.J. (2021). A Unique Carboxylic-Acid Hydrogen-Bond Network (CAHBN) Confers Glutaminyl Cyclase Activity on M28 Family Enzymes. J. Mol. Biol. *433*, 166960. https://doi.org/10.1016/j.jmb.2021.166960.

69. Fan, J., Bellon, M., Ju, M., Zhao, L., Wei, M., Fu, L., and Nicot, C. (2022). Clinical significance of FBXW7 loss of function in human cancers. Mol. Cancer *21*, 87. https://doi.org/10.1186/s12943-022-01548-2.

70. Akhoondi, S., Sun, D., von der Lehr, N., Apostolidou, S., Klotz, K., Maljukova, A., Cepeda, D., Fiegl, H., Dafou, D., Marth, C., et al. (2007). FBXW7/hCDC4 is a general tumor suppressor in human cancer. Cancer Res. *67*, 9006–9012. https://doi.org/10.1158/0008-5472.CAN-07-1320.

71. Tate, J.G., Bamford, S., Jubb, H.C., Sondka, Z., Beare, D.M., Bindal, N., Boutselakis, H., Cole, C.G., Creatore, C., Dawson, E., et al. (2019). COSMIC: the Catalogue Of Somatic Mutations In Cancer. Nucleic Acids Res. *47*, D941–D947. https://doi.org/10.1093/nar/gky1015.

72. Davis, R.J., Gönen, M., Margineantu, D.H., Handeli, S., Swanger, J., Hoellerbauer, P., Paddison, P.J., Gu, H., Raftery, D., Grim, J.E., et al. (2018). Pan-cancer transcriptional signatures predictive of oncogenic mutations reveal that Fbw7 regulates cancer cell oxidative metabolism. Proc. Natl. Acad. Sci. USA *115*, 5462–5467. https://doi.org/10.1073/pnas.1718338115.

73. Xia, H., Dufour, C.R., Medkour, Y., Scholtes, C., Chen, Y., Guluzian, C., B'Chir, W., and Giguère, V. (2023). Hepatocyte FBXW7-dependent activity of nutrient-sensing nuclear receptors controls systemic energy homeostasis and NASH progression in male mice. Nat. Commun. *14*, 6982. https://doi.org/10.1038/s41467-023-42785-3.

74. Carroll, P.A., Diolaiti, D., McFerrin, L., Gu, H., Djukovic, D., Du, J., Cheng, P.F., Anderson, S., Ulrich, M., Hurley, J.B., et al. (2015). Deregulated Myc requires MondoA/Mlx for metabolic reprogramming and tumorigenesis. Cancer Cell *27*, 271–285. https://doi.org/10.1016/j.ccell.2014.11.024.

75. Walker, W., Zhou, Z.Q., Ota, S., Wynshaw-Boris, A., and Hurlin, P.J. (2005). Mnt-Max to Myc-Max complex switching regulates cell cycle entry. J. Cell Biol. *169*, 405–413. https://doi.org/10.1083/jcb.200411013.

76. Cliff, T.S., Wu, T., Boward, B.R., Yin, A., Yin, H., Glushka, J.N., Prestegaard, J.H., and Dalton, S. (2017). MYC Controls Human Pluripotent Stem Cell Fate Decisions through Regulation of Metabolic Flux. Cell Stem Cell *21*, 502–516.e9. https://doi.org/10.1016/j.stem.2017.08.018.

77. Gu, W., Gaeta, X., Sahakyan, A., Chan, A.B., Hong, C.S., Kim, R., Braas, D., Plath, K., Lowry, W.E., and Christofk, H.R. (2016). Glycolytic Metabolism Plays a Functional Role in Regulating Human Pluripotent Stem Cell State. Cell Stem Cell *19*, 476–490. https://doi.org/10.1016/j.stem.2016.08.008.

78. Wilson, A., Murphy, M.J., Oskarsson, T., Kaloulis, K., Bettess, M.D., Oser, G.M., Pasche, A.C., Knabenhans, C., Macdonald, H.R., and Trumpp, A. (2004). c-Myc controls the balance between hematopoietic stem cell self-renewal and differentiation. Genes Dev. *18*, 2747–2763. https://doi.org/10.1101/gad.313104.

79. Wenes, M., Jaccard, A., Wyss, T., Maldonado-Pérez, N., Teoh, S.T., Lepez, A., Renaud, F., Franco, F., Waridel, P., Yacoub Maroun, C., et al. (2022). The mitochondrial pyruvate carrier regulates memory T cell differentiation and antitumor function. Cell Metab. *34*, 731–746.e9. https://doi.org/10.1016/j.cmet.2022.03.013.

80. Petrelli, F., Scandella, V., Montessuit, S., Zamboni, N., Martinou, J.C., and Knobloch, M. (2023). Mitochondrial pyruvate metabolism regulates the activation of quiescent adult neural stem cells. Sci. Adv. *9*, eadd5220. https://doi.org/10.1126/sciadv.add5220.

81. Sanjana, N.E., Shalem, O., and Zhang, F. (2014). Improved vectors and genome-wide libraries for CRISPR screening. Nat. Methods *11*, 783–784. https://doi.org/10.1038/nmeth.3047.

82. Doench, J.G., Fusi, N., Sullender, M., Hegde, M., Vaimberg, E.W., Donovan, K.F., Smith, I., Tothova, Z., Wilen, C., Orchard, R., et al. (2016). Optimized sgRNA design to maximize activity and minimize off-target effects of CRISPR-Cas9. Nat. Biotechnol. *34*, 184–191. https://doi.org/10.1038/nbt.3437.

83. Sanson, K.R., Hanna, R.E., Hegde, M., Donovan, K.F., Strand, C., Sullender, M.E., Vaimberg, E.W., Goodale, A., Root, D.E., Piccioni, F., et al. (2018). Optimized libraries for CRISPR-Cas9 genetic screens with multiple modalities. Nat. Commun. *9*, 5416. https://doi.org/10.1038/s41467-018-07901-8.

84. Skinner, O.S., Blanco-Fernández, J., Goodman, R.P., Kawakami, A., Shen, H., Kemény, L.V., Joesch-Cohen, L., Rees, M.G., Roth, J.A., Fisher, D.E., et al. (2023). Salvage of ribose from uridine or RNA supports glycolysis in nutrient-limited conditions. Nat. Metab. *5*, 765–776. https://doi.org/10.1038/s42255-023-00774-2.

85. Harhai, M., Foged, M.M., Zarges, C., Landoni, J.C., Chollet, S., Simonelli, M., Recazens, E., Lisci, M., Laban, N., Manley, S., et al. (2025). An updated inventory of genes essential for oxidative phosphorylation identifies a mitochondrial origin in familial Meniere's disease. Cell Rep. *44*, 116069. https://doi.org/10.1016/j.celrep.2025.116069.

86. Strefeler, A., Baker, Z.N., Chollet, S., Foged, M.M., Guerra, R.M., Ivanisevic, J., Gallart-Ayala, H., Pagliarini, D.J., and Jourdain, A.A. (2025). Uridine-sensitized screening identifies demethoxy-coenzyme Q and NUDT5 as regulators of nucleotide synthesis. Nat. Metab. *7*, 2221–2235. https://doi.org/10.1038/s42255-025-01419-2.

87. Barretina, J., Caponigro, G., Stransky, N., Venkatesan, K., Margolin, A.A., Kim, S., Wilson, C.J., Lehár, J., Kryukov, G.V., Sonkin, D., et al. (2012). The Cancer Cell Line Encyclopedia enables predictive modelling of anticancer drug sensitivity. Nature *483*, 603–607. https://doi.org/10.1038/nature11003.

88. Kulak, N.A., Pichler, G., Paron, I., Nagaraj, N., and Mann, M. (2014). Minimal, encapsulated proteomic-sample processing applied to copy-number estimation in eukaryotic cells. Nat. Methods *11*, 319–324. https://doi.org/10.1038/nmeth.2834.

89. Wiśniewski, J.R., and Gaugaz, F.Z. (2015). Fast and sensitive total protein and Peptide assays for proteomic analysis. Anal. Chem. *87*, 4110–4116. https://doi.org/10.1021/ac504689z.

90. Meier, F., Brunner, A.D., Koch, S., Koch, H., Lubeck, M., Krause, M., Goedecke, N., Decker, J., Kosinski, T., Park, M.A., et al. (2018). Online Parallel Accumulation-Serial Fragmentation (PASEF) with a Novel Trapped Ion Mobility Mass Spectrometer. Mol. Cell. Proteomics *17*, 2534–2545. https://doi.org/10.1074/mcp.TIR118.000900.

91. Meier, F., Brunner, A.D., Frank, M., Ha, A., Bludau, I., Voytik, E., Kaspar-Schoenefeld, S., Lubeck, M., Raether, O., Bache, N., et al. (2020). diaPASEF: parallel accumulation-serial fragmentation combined with data-independent acquisition. Nat. Methods *17*, 1229–1236. https://doi.org/10.1038/s41592-020-00998-0.

92. Cox, J., Hein, M.Y., Luber, C.A., Paron, I., Nagaraj, N., and Mann, M. (2014). Accurate proteome-wide label-free quantification by delayed normalization and maximal peptide ratio extraction, termed MaxLFQ. Mol. Cell. Proteomics *13*, 2513–2526. https://doi.org/10.1074/mcp.M113.031591.

93. Tyanova, S., Temu, T., Sinitcyn, P., Carlson, A., Hein, M.Y., Geiger, T., Mann, M., and Cox, J. (2016). The Perseus computational platform for comprehensive analysis of (prote)omics data. Nat. Methods *13*, 731–740. https://doi.org/10.1038/nmeth.3901.

94. Perez-Riverol, Y., Bai, J., Bandla, C., García-Seisdedos, D., Hewapathirana, S., Kamatchinathan, S., Kundu, D.J., Prakash, A., Frericks-Zipper, A., Eisenacher, M., et al. (2022). The PRIDE database resources in 2022: a hub for mass spectrometry-based proteomics evidences. Nucleic Acids Res. *50*, D543–D552. https://doi.org/10.1093/nar/gkab1038.

95. Medina, J., van der Velpen, V., Teav, T., Guitton, Y., Gallart-Ayala, H., and Ivanisevic, J. (2020). Single-Step Extraction Coupled with Targeted HILIC-MS/MS Approach for Comprehensive Analysis of Human Plasma Lipidome and Polar Metabolome. Metabolites *10*, 495. https://doi.org/10.3390/metabo10120495.

96. van der Velpen, V., Teav, T., Gallart-Ayala, H., Mehl, F., Konz, I., Clark, C., Oikonomidi, A., Peyratout, G., Henry, H., Delorenzi, M., et al. (2019). Systemic and central nervous system metabolic alterations in Alzheimer's disease. Alzheimers Res. Ther. *11*, 93. https://doi.org/10.1186/s13195-019-0551-7.

97. Gallart-Ayala, H., Konz, I., Mehl, F., Teav, T., Oikonomidi, A., Peyratout, G., van der Velpen, V., Popp, J., and Ivanisevic, J. (2018). A global HILIC-MS approach to measure polar human cerebrospinal fluid metabolome: Exploring gender-associated variation in a cohort of elderly cognitively healthy subjects. Anal. Chim. Acta *1037*, 327–337. https://doi.org/10.1016/j.aca.2018.04.002.

98. Guijas, C., Montenegro-Burke, J.R., Domingo-Almenara, X., Palermo, A., Warth, B., Hermann, G., Koellensperger, G., Huan, T., Uritboonthai, W., Aisporna, A.E., et al. (2018). METLIN: A Technology Platform for Identifying Knowns and Unknowns. Anal. Chem. *90*, 3156–3164. https://doi.org/10.1021/acs.analchem.7b04424.

99. Midani, F.S., Wynn, M.L., and Schnell, S. (2017). The importance of accurately correcting for the natural abundance of stable isotopes. Anal. Biochem. *520*, 27–43. https://doi.org/10.1016/j.ab.2016.12.011.

100. Tsugawa, H., Kanazawa, M., Ogiwara, A., and Arita, M. (2014). MRMPROBS suite for metabolomics using large-scale MRM assays. Bioinformatics *30*, 2379–2380. https://doi.org/10.1093/bioinformatics/btu203.

101. Roci, I., Gallart-Ayala, H., Schmidt, A., Watrous, J., Jain, M., Wheelock, C.E., and Nilsson, R. (2016). Metabolite Profiling and Stable Isotope Tracing in Sorted Subpopulations of Mammalian Cells. Anal. Chem. *88*, 2707–2713. https://doi.org/10.1021/acs.analchem.5b04071.

102. Jain, M., Nilsson, R., Sharma, S., Madhusudhan, N., Kitami, T., Souza, A.L., Kafri, R., Kirschner, M.W., Clish, C.B., and Mootha, V.K. (2012). Metabolite profiling identifies a key role for glycine in rapid cancer cell proliferation. Science *336*, 1040–1044. https://doi.org/10.1126/science.1218595.

Please cite this article in press as: Lisci et al., Functional nutrient-genetic profiling reveals biotin and FBXW7 are essential to bypass glutamine addiction, Molecular Cell (2026), https://doi.org/10.1016/j.molcel.2026.02.002

STAR★METHODS

KEY RESOURCES TABLE

REAGENT or RESOURCE	SOURCE	IDENTIFIER
Antibodies		
Mouse monoclonal anti-FLAG® (clone: M2)	Sigma-Aldrich	Cat# F1804; RRID: AB_262044
Rabbit polyclonal anti-GLAST/EAAT1 (SLC1A3)	Proteintech	Cat# 20785-1-AP; RRID: AB_2878738
Rabbit monoclonal anti-xCT/SLC7A11 (clone: D2M7A)	Cell Signaling Technology	Cat# 12691; RRID: AB_2687474
Rabbit monoclonal anti-ATF4 (clone: D4B8)	Cell Signaling Technology	Cat# 11815; RRID: AB_2616025
Mouse monoclonal anti-GOT1 (clone: 5A12E10)	Proteintech	Cat# 60317-1-Ig; RRID: AB_2881428
Mouse monoclonal anti-MDH1 (clone: 1F9A2)	Proteintech	Cat# 66505-1-Ig; RRID: AB_2881868
Rabbit polyclonal anti-PC	Sigma-Aldrich	Cat# HPA043922; RRID: AB_2678732
Rabbit polyclonal anti-FBXW7	Bethyl Laboratories	Cat# A301-721A; RRID: AB_1210898
Mouse monoclonal anti-c-MYC (clone: 9E10)	Santa Cruz	Cat# sc-40; RRID: AB_627268
Rabbit polyclonal anti-MNT	Proteintech	Cat# 23742-1-AP; RRID: AB_2879314
Mouse monoclonal anti-SIN3A (clone: 2B12E8)	Proteintech	Cat# 67197-1-Ig; RRID: AB_2882490
Mouse monoclonal anti-MLX (clone: 2A8D2)	Proteintech	Cat# 67042-1-Ig; RRID: AB_2882356
Mouse monoclonal anti-MLXIP (clone: 2E11A4)	Proteintech	Cat# 68977-1-Ig; RRID: AB_3670457
Rabbit polyclonal anti-β-actin	Sigma-Aldrich	Cat# A2066; RRID: AB_476693
IRDye 800CW Goat anti-rabbit	LICORbio	Cat# 926-3211; RRID: AB_621843
IRDye 680RD Goat anti-mouse	LICORbio	Cat# 926_68070; RRID: 10956588
Rabbit IgG polyclonal isotope control (ChIP grade)	Abcam	Cat# ab171870; RRID: AB_2687657
Rabbit polyclonal anti-MAX	Novus Biotechne	Cat# NBP1-88624; RRID: AB_11019874
Rabbit polyclonal anti-MNT (ChIP)	Bethyl Laboratories	Cat# A303-627A; RRID: AB_11205638
Rabbit polyclonal anti-SIN3A (ChIP)	Novus Biotechne	Cat# NB600-1263; RRID: AB_2187631
Rabbit polyclonal anti-H3K27Ac (ChIP grade)	Abcam	Cat# ab4729; RRID: AB_2118291
Hamster monoclonal anti-CD3e (clone: eBio500A2) functional grade, eBioscience™	ThermoFisher	Cat# 16-0033-86; RRID: AB_842782
Hamster monoclonal anti-CD28 (clone: 37.51) functional grade, eBioscience™	ThermoFisher	Cat# 16-0281-82; RRID: AB_468921
Bacterial and virus strains		
One Shot® Stbl3™ Chemically Competent E. coli	Invitrogen	Cat# C7373-03
Chemicals, peptides, and recombinant proteins		
DMEM high glucose (with GlutaMAX™ I, 4500 mg/L D-Glucose, Sodium Pyruvate)	Invitrogen	Cat# 31966021
DMEM no glucose, no glutamine, no pyruvate, no phenol red	Gibco	Cat# A14430
RPMI 1640, GlutaMAX™ supplement	Invitrogen	Cat# 61870010
Fetal bovine serum	FisherScientific	Cat# 17479633
Fetal bovine serum, dialyzed	Sigma-Aldrich	Cat# F0392
Penicillin/streptomycin	Bioconcept	Cat# 4-01F00-H
D-(+)-Glucose	Sigma-Aldrich	Cat# G7021
Sodium pyruvate	ThermoFisher	Cat# 11360070
L-glutamine	Amimed	Cat# 5-10K00-H
L-glutamic acid monosodium hydrate	Sigma-Aldrich	Cat# G5889
L-alanine	Sigma-Aldrich	Cat# A7469
D-alanine	Sigma-Aldrich	Cat# A7377

(*Continued on next page*)

Please cite this article in press as: Lisci et al., Functional nutrient-genetic profiling reveals biotin and FBXW7 are essential to bypass glutamine addiction, Molecular Cell (2026), https://doi.org/10.1016/j.molcel.2026.02.002

Continued

REAGENT or RESOURCE	SOURCE	IDENTIFIER
Diethyl succinate	Sigma-Aldrich	Cat# 112402
2-ketobutyric acid	Sigma-Aldrich	Cat# K401
Dimethyl 2-oxoglutarate	Sigma-Aldrich	Cat# 349631
Thymidine	Sigma-Aldrich	Cat# T1895
L-aspartic acid	Sigma-Aldrich	Cat# A8949
L-asparagine monohydrate	Sigma-Aldrich	Cat# A4284
Uridine	Sigma-Aldrich	Cat# U3003
Biotin	Sigma-Aldrich	Cat# B4639
β-mercaptoethanol	PAN-Biotech	Cat# P07-05020
Puromycin	Invivogen	Cat# ant-pr-1
Blasticidin	Sigma-Aldrich	Cat# SBR00022
4-hydroxytamoxifen	MedChemExpress	Cat# HY-16950
UK5099	MedChemExpress	Cat# HY-15475
Sulfasalazin	Sigma-Aldrich	Cat# S0883
Bafilomycin	MedChemExpress	Cat# HY-100558
PFI7	Structural Genomics Consortium	Free sample
ISRIB	Sigma-Aldrich	Cat# SML0843
Actinomycin D	Sigma-Aldrich	Cat# A9415
Polybrene	Sigma-Aldrich	Cat# TR-1003G
Murine IL-2 recombinant protein, PeproTech®	ThermoFisher (Gibco)	Cat# 212-12
cOmplete™ ULTRA protease inhibitor tablets	Roche	Cat# 05892970001
Pierce™ Universal Nuclease	Life Technologies	Cat# 88702
Sodium deoxycholate	Sigma-Aldrich	Cat# D6750
IGEPAL® CA-630 (NP40 analog)	Sigma-Aldrich	Cat# I8896
TRI reagent	Sigma-Aldrich	Cat# T3809
M-MLV Reverse Transcriptase	Sigma-Aldrich	Cat# M1302-40KU
RnaseOut Recombinant RNase Inhibitor	Invitrogen	Cat# 10777019
Random hexamers	ThermoFisher	Cat# N8080127
RNAse A	Takara Bio	Cat# 740505
Proteinase K	Sigma-Aldrich	Cat# SRE0005
Phenol-chloroform-isoamyl alcohol	Sigma-Aldrich	Cat# 77617
IRDye® 680RD Streptavidin	LICORbio	Cat# 926-68079
Critical commercial assays		
NucleoSpin Blood kit	Machery Nagel	Cat# 740954.20
DC Protein Assay	Bio-Rad	Cat# 5000111
Pierce High pH Reversed-Phase Peptide Fractionation Kit	ThermoFisher	Cat# 84868
PM-M1	BioLog	Cat# 13101
PM-M2	BioLog	Cat# 13102
PM-M3	BioLog	Cat# 13103
PM-M4	BioLog	Cat# 13104
BioLog MA dye	BioLog	Cat# 74351
PrestoBlue™ Cell Viability Reagent	Life Technologies	Cat# A13262
CellTiter-Glo® 2.0 Cell Viability Assay	Promega	Cat# G9242
$CD8a^+$ T cell isolation kit, mouse	Miltenyi Biotec	Cat# 130-104-075

(*Continued on next page*)

Please cite this article in press as: Lisci et al., Functional nutrient-genetic profiling reveals biotin and FBXW7 are essential to bypass glutamine addiction, Molecular Cell (2026), https://doi.org/10.1016/j.molcel.2026.02.002

Continued

REAGENT or RESOURCE	SOURCE	IDENTIFIER
Deposited data		
^{13}C- and ^{15}N-glutamine isotopic profiling in K562; ^{13}C-pyruvate isotopic profiling in primary CD8^{+} T cells	This study	MTBLS13799
^{13}C-pyruvate isotopic profiling in K562	This study	14002048
Multiple pathway targeted analysis of polar metabolites	This study	14002048
Mass spectrometry data	This study	PXD057389
Spheroid imaging data	This study	https://www.doi.org/10.17632/328g7zyt9d.1
K562 RNAseq	Slavoff et al.[81]	GSE34740
Transcription factor ChIP-seq in K562	ENCODE[68]	MYC(ENCFF801QJW), MNT(ENCFF611RGV), SIN3A(ENCFF085NLG)
H3K27ac ChIP-seq in K562	ENCODE[68]	ENCFF381NDD
Experimental models: Cell lines		
Human: K562	American Type Culture Collection (ATCC)	Cat# CCL-243; RRID: CVCL_0004
Human: HEK293T	ATCC	Cat# CRL-3216; RRID: CVCL_0063
Human: HeLa	ATCC	Cat# CCL-2; RRID: CVCL_0030
Human: MCF-7	ATCC	Cat# HTB-22; RRID: CVCL_0031
Human: SW480	ATCC	Cat# CCL-228; RRID: CVCL_0546
Human: UACC-257	Frederick Cancer Division of Cancer Treatment and Diagnostic (DCTD)	RRID: CVCL_1779
Human: U-2 OS	ATCC	Cat# HTB-96; RRID: CVCL_0042
Human: A375	ATCC	Cat# CRL-1619; RRID: CVCL_0132
Mouse: MC38	Sigma-Aldrich	Cat# SCC172; RRID: CVCL_B288
Mouse: B16-F10	ATCC	Cat# CRL-6475; RRID: CVCL_0159
Mouse: MycER mouse embryonic fibroblast	Wise et al.[9]; Linder et al.[19]	N/A
Oligonucleotides		
sgRNAs, see Table S9	Integrated DNA Technologies	N/A
ChIP primers, see Table S9	Integrated DNA Technologies	N/A
Random hexamers	ThermoFisher	Cat# N8080127
TaqMan Gene Expression Assay, human PC, FAM-MGB	Life Technologies	Cat# Hs01085875_g1
Taqman Gene Expression Assay, human TBP, VIC-MGB	Life Technologies	Cat# Hs00427620_m1
Recombinant DNA		
pLX304-GFP-V5	Kim et al.[82]	Addgene, Cat# 193687; RRID: Addgene_193687
pLX304-PC	Wiemann et al.[83]	DNAsu, Cat# HsCD00436386
pWPI-Neo-GFP-3xFLAG	Jourdain et al.[84]	Addgene, Cat# 201639; RRID: Addgene_201639
pWPI-SLC7A11-HA	Jourdain et al.[84]	Addgene, Cat# 201643; RRID: Addgene_201643
pMXS-SLC1A3	Birsoy et al.[30]	Addgene, Cat# 72873; RRID: Addgene_72873
pLVX-TetOne-Puro-GFP-3xFLAG	This study	N/A
pLVX-TetOne-Puro-LbNOX	Titov et al.[31] and Choe et al.[85]	Addgene, Cat# 234984; RRID: Addgene_234984
pTwist-Lenti-CMV-BSD-GFP-3xFLAG	This study	Twist Bioscience
pTwist-Lenti-CMV-BSD-PC-WT	This study	Twist Bioscience
pTwist-Lenti-CMV-BSD-PC-K1144R	This study	Twist Bioscience
pTwist-Lenti-CMV-Puro-FBXW7-WT	This study	Twist Bioscience
pTwist-Lenti-CMV-Puro-FBXW7-R465C	This study	Twist Bioscience

(*Continued on next page*)

Please cite this article in press as: Lisci et al., Functional nutrient-genetic profiling reveals biotin and FBXW7 are essential to bypass glutamine addiction, Molecular Cell (2026), https://doi.org/10.1016/j.molcel.2026.02.002

Continued

REAGENT or RESOURCE	SOURCE	IDENTIFIER
pTwist-Lenti-CMV-Puro-FBXW7-R505C	This study	Twist Bioscience
pTwist-Lenti-CMV-Puro-FBXW7-R479Q	This study	Twist Bioscience
psPAX2	Didier Trono	Addgene, Cat# 12260; RRID: Addgene_12260
pMD2.G	Didier Trono	Addgene, Cat# 12259; RRID: Addgene_12259
lentiCRISPR v2	Sanjana et al.[86]	Addgene, Cat# 52961; RRID: Addgene_52961
Human sgRNA library Brunello (lentiCRISPR v2)	Sanson et al.[87]	Addgene, Cat# 73179; RRID: Addgene_73179
Software and algorithms		
Prism	GraphPad Software	https://www.graphpad.com/
Fiji	Schindelin et al.[88]	https://imagej.net/software/fiji/
IGV	Robinson et al.[89]	https://igv.org/
GSEA	Subramanian et al.[90]	https://www.gsea-msigdb.org/gsea/index.jsp
MetaboAnalyst	Pang et al.[29]	https://www.metaboanalyst.ca/
Spectronaut	Biognosys Schlieren	https://biognosys.com/software/spectronaut/
IDPicker algorithm	Ma et al.[91]	https://proteowizard.sourceforge.io/idpicker/
MaxLFQ algorithm	Cox et al.[92]	https://www.maxquant.org/
Perseus	Tyanova et al.[93]	https://maxquant.net/perseus/
MassHunter Quantitative Analysis	Agilent Technologies	https://www.agilent.com/en/product/software-informatics/mass-spectrometry-software
ProFinder	Agilent Technologies	https://www.agilent.com/en/product/software-informatics/mass-spectrometry-software/data-analysis/mass-profiler-professional-software
R	R Core Team[94]	http://cran.r-project.org/
LOWESS/Spline normalization algorithm	Tsugawa et al.[95]	http://prime.psc.riken.jp
Xcalibur	ThermoFisher	https://www.thermofisher.com/us/en/home/industrial/mass-spectrometry/liquid-chromatography-mass-spectrometry-lc-ms/lc-ms-software/lc-ms-data-acquisition-software/xcalibur-data-acquisition-interpretation-software.html
Compound Discoverer	ThermoFisher	https://www.thermofisher.com/ch/en/home/industrial/mass-spectrometry/liquid-chromatography-mass-spectrometry-lc-ms/lc-ms-software/multi-omics-data-analysis/compound-discoverer-software.html?cid=E.25CMD.CD103.25418.01
Skyline	University of Washington	https://skyline.ms/home/software/Skyline/project-begin.view
Other		
U-bottom Nunclon™ Sphera™ 96-Well plates	ThermoFisher	Cat# 174925
Nunc™ MicroWell™ 96-Well plates	Nunc	Cat# 137101
8-16% Novex™ WedgeWell™ Tris-Glycine gels	ThermoFisher	Cat# XP08160BOX
Dynabeads Protein G	ThermoFisher	Cat# 10007D
Dynabeads Protein A	ThermoFisher	Cat# 10001D

EXPERIMENTAL MODEL AND STUDY PARTICIPANT DETAILS

Cell lines

K562 (ATCC, CCL-243), HEK293T (ATCC, CRL-3216, referred to as 293T), HeLa (ATCC, CCL-2), MCF7 (ATCC, HTB-22), SW480 (ATCC, CCL-228), UACC-257 (DCTD, CVCL_1779), U-2 OS (ATCC, HTB-96), A375 (CRL-1619), MC38 (CRL-2640) and B16-F10 (CRL-6475) were maintained under standard cell culture conditions in DMEM containing 25 mM glucose, 1 mM sodium pyruvate, 2 mM glutamine, and supplemented with 10% fetal bovine serum (FBS) and 100 U/mL penicillin/streptomycin. MC38 cells were additionally supplemented with 0.1 mM NEAA, 10 mM Hepes and 50 μg/ml gentamycin. MycER mouse embryonic fibroblasts were a kind gift from Raul Mostoslavsky (Harvard Medical School) and were cultured in DMEM supplemented with glucose, pyruvate, glutamine, FBS and penicillin/streptomycin as indicated above. Myc expression was induced by supplementing the cell culture medium with 200 nM 4-hydroxytamoxifen (4-OHT) (MedChemExpress, HY-16950). All cells were cultured at 37°C, 5% CO_2 and regularly tested to ensure the absence of mycoplasma.

Primary cells

Primary murine $CD8^+$ T cells were isolated from wild-type mice (C57BL/6J) that were bred and housed at the animal facility at CHUV/UNIL Laboratory Center of Epalinges (Centre Laboratoire d'Epalinges, CLE, license n. VD3788). Spleens were extracted from three 10 weeks-old males, and splenocytes were activated on plate-bound 0.5 μg/ml hamster anti-mouse CD3 clone eBio500A2 (ThermoFisher, 16-0033-86) and 1μg/ml hamster anti-mouse CD28 clone 37.51 (ThermoFisher, 16-0281-82). $CD8^+$ T cells were purified 48 h post-stimulation using the mouse $CD8a^+$ T cell Isolation Kit (MACS Miltenyi Biotec, 130-104-075), following manufacturer's instructions. Primary $CD8^+$ T cells were cultured in RPMI medium with L-glutamine and sodium bicarbonate (Sigma-Aldrich, 1640) supplemented with 10% heat-inactivated FBS, 100 U/mL penicillin/streptomycin, 1 mM sodium pyruvate, 50 μM β-mercaptoethanol (PAN Biotech, P07-05020) and 100 U/mL murine IL-2 (ThermoFisher/Gibco, 212-12). Cells were cultured at at 37°C, 5% CO_2.

METHOD DETAILS

Spheroid culture

5,000 HEK293T cells per well were seeded on U-bottom Nunclon™ Sphera™ 96-Well plates (ThermoFisher, 174925) in 200 μL of glucose-free and glutamine-free DMEM supplemented with 25 mM glucose, 10% dialyzed FBS, and 100 U/mL penicillin/streptomycin. Experimental media were supplemented with either 2 mM pyruvate or 2 mM glutamine, as indicated. The plates were then briefly centrifuged to allow cells to settle at the bottom of the well. Spheroids formed spontaneously and samples were imaged every 3-4 days with an EVOSTM FL imaging system (Life Technologies) with a 4x objective or with an Incucyte® S3 Live-Cell Analysis System (Sartorius) with a 4x objective. Spheroid diameter was quantified using Fiji (ImageJ). For biotin and pyruvate supplementation, HEK293T cells were first cultured in standard DMEM (25 mM glucose, 1 mM pyruvate, 2 mM glutamine) supplemented with 100 U/mL penicillin/streptomycin and 10% dialyzed FBS for two weeks to deprive cells of biotin. After 14 days, HEK293T cells were seeded in in glucose-free and glutamine-free DMEM containing 25 mM glucose and supplemented with 10% dialyzed FBS and 100 U/mL penicillin/streptomycin and treated as above. Test media were prepared with the addition of either 2 mM of pyruvate, 1 μM of biotin, or both, as indicated in the figure legends. Raw spheroid imaging data was deposited on Mendeley Data: https://10.17632/328g7zyt9d.1).

Proliferation assays

To measure proliferation, cells were cultured in DMEM lacking glucose, glutamine, pyruvate and phenol red (Gibco, A14430) supplemented with 10% dialyzed FBS, 100 U/mL penicillin/streptomycin and 25 mM glucose. Cells were seeded at 1 x 10^5/mL in black Nunc™ MicroWell™ 96-Well plates (NUNC, 137101) for the Prestoblue assay, or in flat-bottom 12-well plates for standard cell and viability count. Test media were supplemented with 2 mM glutamine, 2 mM pyruvate, or 2 mM of all other amino acids or carboxylic acid as indicated, except for aspartate and asparagine, which were added at a final concentration of 150 μM as previously described.[25] Proliferation was measured after 4-5 days either by trypan-blue mediated count (Vi-cell blu counter, Beckman Coulter), or by adding the Prestoblue dye (Life Technologies, A13262) and measuring fluorescence (excitation: 560 nm, emission: 590 nm), or by using the CellTiter-Glo dye (Promega, G9242) and measuring luminescence, with the last two performed using a BioTek Synergy plate reader (Agilent). "Relative growth" was quantified by normalizing proliferation to the internal control sample (complete media, untreated cells, or sgCtrl as indicated in the figure legends). For drug treatments, the following inhibitors were added to the cell culture medium at the beginning of each growth assay: 375 μM sulfasalazine; 100 nM ISRIB; 5 μM bafilomycin; 50 nM PFI-7. All proliferation assays reported in the main figures were performed with the Prestoblue assay.

Cloning and lentiviral infection

Gene-specific guides (sgRNA) were selected from the two best sequences as scored in the CRISPR-Cas9 screen and were ordered as complementary oligonucleotides (Integrated DNA Technologies, IDT). sgRNAs were cloned into the pLentiCRISPR v2 vector (Addgene, 52961) using the BsmBI site. Two guides targeting olfactory receptors not expressed in K562, *OR2M4* and *OR11A1*,

were used to generate vectors for the negative control (sgCtrl) samples. Lentiviruses were produced in HEK293T cultures as previously described,[81] and K562 cells were infected in the presence of 10 μg/ml polybrene (Sigma-Aldrich, TR-1003G). Successfully infected K562 were selected after 24 h using 2 μg/mL puromycin or 100 μg/mL blasticidin. Cells were counted 3 days post-selection and maintained in standard cell culture medium as described above for 10-12 days before analysis to ensure gene knockout and target protein degradation, or 7 days for overexpression, both of which were confirmed by immunoblotting. sgRNA sequences are described in Table S9.

Genome-wide CRISPR-Cas9 screen

We infected K562 cells in duplicates with the Brunello lentiviral genome-wide CRISPR-Cas9 library (Genome Perturbation Platform, Broad Institute) containing 76,441 single-guide RNAs (sgRNAs) targeting 19,114 distinct human genes and 1,000 controls[82,83] as previously described.[84] Infection was performed at a multiplicity of infection of 0.3, using 500 cells per sgRNA guide, and in the presence of 10 μg/mL polybrene (Sigma-Aldrich, TR-1003G). Successfully infected cells were selected after 24 h using 2 μg/mL puromycin. After 10 days to allow for CRISPR-Cas9-mediated gene knockout, cells were plated at 1 x 10^5/mL (equivalent to 1000 cells per sgRNA for the glutamine-rich condition, and 2000 cells per sgRNA for the glutamine-depleted condition) in DMEM medium supplemented with 10% dialyzed FBS, 100 U/mL penicillin/streptomycin, 25 mM glucose, 50 μg/mL uridine, and either 2 mM glutamine or water as a negative control. Cells were cultured for 3 weeks and harvested on day 31 post-infection. The NucleoSpin Blood kit (Machery Nagel, 740954.20) was used to extract total genomic DNA, which was subsequently used for barcode sequencing, mapping, and read count at the Genome Perturbation Platform (Broad Institute). This screen was performed in parallel two other screens published by our group.[85,86]

Screen results were analyzed as previously outlined[26] using normalized Z scores. In brief, raw sgRNA read counts were normalized to reads/million and $\log_2$ transformed. The mean $\log_2$(fold change) was calculated based on read counts in the pre-swap control (day 7 post-infection) and averaging the abundance of four sgRNAs. Results were averaged based on the mean across two replicates. The DepMap 24Q2 dataset[87] was used to filter out genes not expressed in K562 (Transcripts per million, TPM < 1) and to define the mean and standard deviation of the null distribution (for each medium condition) and to define Z scores based on this distribution. We calculated the essentiality of each gene by computing the differences between the Z-score in glutamine-depleted (Z_{-Gln}) and glutamine-rich (Z_{+Gln}) media ($\Delta Z = Z_{-Gln} - Z_{+Gln}$). We scored genes showing $\Delta Z < 0$ as "required" and $\Delta Z > 0$ as "detrimental" for growth in glutamine-deprived conditions.

BioLog nutrient screen

Cells were seeded at 1 x 10^5/mL in the PM-M1, PM-M2, PM-M3, and PM-M4 BioLog plates (Biolog, PM-M1: 13101, PM-M2: 13102, PM-M3: 13103, PM-M4: 13104) in DMEM containing 25 mM glucose and supplemented with 10% dialyzed FBS and 100 U/mL penicillin/streptomycin. Samples were cultured for 4 days at 37°C, 5% CO_2. Cell growth was measured using the BioLog MA dye (Biolog, 74351) by quantifying absorbance at 590 nm using a SpectraMax ID3 plate reader (Molecular Devices).

Immunoblotting

Cells were washed in ice-cold PBS and flash-frozen on dry ice as pellets. Samples were lysed in RIPA buffer (25 mM Tris pH 7.5, 150 mM NaCl, 0.1% SDS, 0.1% sodium deoxycholate, 1% NP40 analog) supplemented with cOmplete™ ULTRA protease inhibitor tablets (Roche, 05892970001) and Pierce™ Universal Nuclease (Life Technologies, 88702) by incubation on ice for 20 min. Supernatants were cleared by spinning samples for 10 min at 14,000 *g* at 4°C. Protein concentration was quantified using the DC Protein Assay (Bio-Rad). Lysates were loaded on 8-16% Novex™ WedgeWell™ Tris-Glycine gels (ThermoFisher, XP08160BOX) and run at 200 V for 1 h. Samples were transferred to nitrocellulose membranes using a wet transfer chamber overnight at 4°C (60 V). Membranes were blocked in 5% milk diluted in TBS + 0.1% Tween (TBS-T) and incubated with a 1:500-1:1000 dilution of primary antibody for 1.5 h at room temperature (or overnight at 4°C), then with a secondary antibody at 1:10,000 dilution for 1 h at room temperature. All antibodies were diluted in 5% milk in TBS-T. For streptavidin probing, membranes were blocked in 5% bovine serum albumin (BSA) in TBS-T and incubated with 1:5000 IRDye® 680RD Streptavidin (LICORbio, 926-68079) for 40 min at room temperature. All washes were performed in TBS-T, and membranes were imaged using fluorescence detection on an Odyssey CLx analyzer (LICORbio).

RNA extraction, cDNA synthesis and qPCR

Total RNA was extracted in phenol/chloroform using TRI reagent (Sigma-Aldrich, T3809), as described by the manufacturer. Complementary DNA (cDNA) was synthesized using random primers (ThermoFisher, N8080127) and M-MLV Reverse Transcriptase (Sigma-Aldrich, M1302-40KU) in the presence of RNAseOUT Recombinant RNAse inhibitor (Invitrogen, 10777019). Quantitative PCR (qPCR) was performed using Taqman probes (see key resources table) and a CFx96 quantitative PCR machine (Bio-Rad). All data were internally normalized to *TBP* expression using the ΔΔCt method.

For mRNA decay analysis, cells were treated with 1 μg/mL actinomycin D (Sigma-Aldrich, A9415) and harvested at the indicated time points. Total RNA extraction, cDNA synthesis, and qPCR were performed as described above. Relative mRNA decay was quantified by normalizing ΔΔCt values at each time point to the initial ΔΔCt (t=0, untreated cells).

Chromatin immunoprecipitation (ChIP)-qPCR

For chromatin isolation, 1 x 10^7 cells were harvested per sample, washed in PBS, and fixed in 1% formaldehyde for 10 (H3K27Ac), 20 (MAX, SIN3A) or 30 (MNT) min at room temperature. Samples were quenched using 125 mM glycine, washed in PBS, lysed in ChIP Lysis buffer (50 mM Hepes-KOH pH 7.5, 140 mM NaCl, 1 mM EDTA pH 8, 1% Triton X-100, 0.1% sodium deoxycholate, and 0.1% SDS), and sonicated using a Bioruptor (Diagenode) to obtain 100-300 bp fragments. Lysates were cleared by centrifugation at maximum speed for 10 min at 4°C, and an aliquot from each was retained as the input sample.

For chromatin immunoprecipitation, lysates were incubated overnight at 4°C with 5 μg IgG control (Abcam, ab171870) or 5 μg of ChIP antibodies anti-MAX (Novus Biotechne, NBP1-88624), anti-MNT (Bethyl, A303-627A), anti-SIN3A (Novus Biotechne, NB600-1263), or anti-H3K27Ac (Abcam, ab4729). The next day, samples were incubated with protein G (MNT, SIN3A, H3K27Ac) or protein A (MAX) beads (previously blocked in 10% bovine serum) for 2 h at room temperature. Beads were washed using wash buffer (20 mM Tris-HCl pH 8, 150 mM NaCl, 2 mM EDTA pH 8, 1% Triton X-100, 0.1% SDS). The final wash was performed with a higher salt concentration (500 mM NaCl) to improve the signal-to-noise ratio. After elution, samples were treated with RNAse A (Takara Bio, 740505) for 1 h at 37°C and proteinase K (Sigma-Aldrich, SRE0005) first for 1 h at 55°C, then overnight at 65°C to remove contaminants. DNA cleanup was performed using phenol-chloroform-isoamyl alcohol (Sigma-Aldrich, 77617) as described by the manufacturer.

For qPCR, primers were designed using the NCBI genome data viewer (https://www.ncbi.nlm.nih.gov/gdv/) and the Integrative Genomic Viewer (IGV) software, GRCh38.p14 Primary Assembly. Oligonucleotides were obtained via Integrated DNA Technologies (IDT). qPCR was performed using primers for the promoter of the *PC* gene, as well as primers for genes showing low (*MYOD*) or high (*GAPDH*, *ALDOA*) levels of H3K27Ac in K562 cells as controls. Data was normalized to the signal in the input sample using the ΔΔCt method. A list of primers used for ChIP-qPCR is provided in Table S9.

Protein mass spectrometry

Protein mass spectrometry was performed at the Protein Analysis Facility at the University of Lausanne. Samples were lysed in 250 μL miST lysis buffer (1% Sodium deoxycholate, 100 mM Tris pH 8.6, 10 mM DTT), heated for 10 min at 75°C, and digested following a modified version of the iST method.[88] Based on tryptophan fluorescence quantification,[89] 100 μg of proteins at 2 μg/μl in miST buffer were heated for 5 min at 95°C, diluted 1:1 (v:v) with water containing 4 mM $MgCl_2$ and 250 Units/μL benzonase (Merck, 70746), and incubated for 15 min at room temperature to digest nucleic acids. Reduced disulfides were alkylated by adding one fourth of the vol. of 160 mM chloroacetamide (32 mM final) and incubating for 45 min at room temperature in the dark. Samples were adjusted to 3 mM EDTA and digested with 1 μg Trypsin/LysC mix (Promega, V5073) for 1 h at 37°C, then for 1 h with an additional 0.5 μg of proteases. To remove sodium deoxycholate, two sample volumes of isopropanol containing 1% TFA were added to the digests, and the samples were desalted on a strong cation exchange (SCX) plate (Oasis MCX; Waters Corp., Milford, MA) by centrifugation. After washing with isopropanol/1%TFA, peptides were eluted in 200 μl of 80% MeCN, 19% water, 1% (v/v) ammonia, and dried by centrifugal evaporation.

Aliquots (1/8) of each sample were pooled and separated into 6 fractions by off-line basic reversed-phase (bRP) using the Pierce High pH Reversed-Phase Peptide Fractionation Kit (ThermoFisher). The fractions were collected in 7.5, 10, 12.5, 15, 17.5, and 50% acetonitrile in 0.1% triethylamine (~pH 10). Dried bRP fractions were redissolved in 50 μL 2% acetonitrile with 0.5% TFA, and 5 μL were injected for LC-MS/MS analyses. LC-MS/MS analyses were carried out on a TIMS-TOF Pro (Bruker, Bremen, Germany) mass spectrometer interfaced through a nanospray ion source (“captive spray”) to an Ultimate 3000 RSLCnano HPLC system (Dionex). Peptides were separated on a reversed-phase custom packed 45 cm C18 column (75 μm ID, 100Å, Reprosil Pur 1.9 μm particles, Dr. Maisch, Germany) at a flow rate of 0.250 μL/min with a 2-27% acetonitrile gradient in 93 min followed by a ramp to 45% in 15 min and to 90% in 5 min (total method time: 140 min, all solvents contained 0.1% formic acid). Identical LC gradients were used for DDA and DIA measurements.

For creation of the spectral library, data-dependent acquisitions (DDA) were carried out on the 6 bRP fractions sample pool using a standard TIMS PASEF method[90] with ion accumulation for 100 ms for each survey MS1 scan and the TIMS-coupled MS2 scans. Duty cycle was kept at 100%. Up to 10 precursors were targeted per TIMS scan. Precursor isolation was done with a 2 Th or 3 Th window below or above m/z 800, respectively. The minimum threshold intensity for precursor selection was 2500. If the inclusion list allowed it, precursors were targeted more than once to reach a minimum target total intensity of 20’000. Collision energy was ramped linearly based uniquely on the 1/k0 values from 20eV (at 1/k0=0.6) to 59 eV (at 1/k0=1.6). Total duration of a scan cycle, including one survey and 10 MS2 TIMS scans, was 1.16 s. Precursors could be targeted again in subsequent cycles if their signal increased by a factor of 4.0 or more. After selection in one cycle, precursors were excluded from further selection for 60 s. Mass resolution in all MS measurements was approximately 35’000. The data-independent acquisition (DIA) used essentially the same instrument parameters as the DDA method reported previously.[91] Per cycle, the mass range 400-1200 m/z was covered by a total of 32 windows, each 25 Th wide and a 1/k0 range of 0.3. Collision energy and resolution settings were the same as in the DDA method. Two windows were acquired per TIMS scan (100 ms) so that the total cycle time was 1.7 s.

Raw Bruker MS data were processed with Spectronaut 16.2 (Biognosys, Schlieren, Switzerland). A library was constructed from the DDA bRP fraction data by searching the annotated human proteome SWISSPROT database of January 7th, 2022 (20’375 sequences). For identification, peptides of 7-52 AA length were considered, cleaved with trypsin/P and a maximum of 2 missed cleavages were allowed. Carbamidomethylation of cysteine (fixed), methionine oxidation and N-terminal protein acetylation (variable) were the modifications applied. Mass calibration was dynamic and based on a first database search. The Pulsar engine was used for

peptide identification. Protein inference was performed with the IDPicker algorithm. Spectra, peptide and protein identifications were all filtered at 1% false discovery rate (FDR) against a decoy database. Specific filtering for library construction removed fragments corresponding to less than 3 AA and fragments outside the 300-1800 m/z range. Only fragments with a minimum base peak intensity of 5% were kept. Precursors with fewer than 3 fragments were also eliminated, and only the best 6 fragments were kept per precursor. No filtering was done on the basis of charge state, and a maximum of 2 missed cleavages was allowed. Shared (non-proteotypic) peptides were kept. The created library contained 110'276 precursors mapping to 83'238 stripped sequences, of which 79'395 were proteotypic. These corresponded to 7,502 protein groups (7,613 proteins). Of these, 806 were single hits (one peptide precursor). In total, 649,960 fragments were used for quantitation. Peptide-centric analysis of DIA data was done with Spectronaut 16.2 using the library described above. Single-hit proteins (defined as being matched by one stripped sequence only) were kept in the Spectronaut analysis. Peptide quantitation was based on XIC area, for which a minimum of 1 and a maximum of 3 (the 3 best) precursors were considered for each peptide, from which the median value was selected. Quantities for protein groups were derived from inter-run peptide ratios based on the MaxLFQ algorithm.[92] Global normalization of runs/samples was done based on the median of peptides. Overall, 105,024 precursors were quantified in the dataset, mapping to 7,190 protein groups. 96,612 precursors (6,889 protein groups) had full profiles, i.e., were quantified in all samples. The average number of data points per peak was 7.4.

Subsequent analyses were done with the Perseus software package (version 1.6.15.0).[93] Contaminant proteins were removed, and quantity values were $\log_2$-transformed. After assignment to groups, only proteins quantified in at least 3 samples of the single-hit group were kept. Volcano plots were generated on Prism (GraphPad Software) after Benjamini-Hochberg false discovery rate (FDR) correction. The mass spectrometry proteomics data have been deposited to the ProteomeXchange Consortium via the PRIDE[94] partner repository with the dataset identifier PXD057389.

Multiple pathway metabolomics analysis of polar metabolites

Metabolomics analysis was performed at the Metabolomics Platform at the University of Lausanne. Cell pellets were extracted with 80% methanol, sonicated and homogenized (Precellys Cryolys). Lysates were centrifuged at 15,000 rpm at 4°C for 15 min, evaporated to dryness and reconstituted in methanol, based on total protein content (quantified by prior BCA assay). Samples were analyzed by liquid chromatography coupled to mass spectrometry (LC-MS/MS) following previously described methods.[95]

For metabolite relative quantification, ultra-high performance liquid chromatography coupled to tandem mass spectrometry (UHPLC-MS/MS) was used, and a Triple Quadrupole mass spectrometer (6495 iFunnel Agilent) in multiple reaction monitoring (MRM) mode was employed for targeted measurement, as previously detailed.[95,96] Metabolome coverage was maximized by using two liquid chromatography modes coupled to positive and negative electrospray ionization MS.[97]

Raw LC-MS/MS data were analyzed using Agilent Quantitative analysis software version B.07.00 (MassHunter Agilent Technologies). Extracted Ion Chromatogram (EIC) areas were used for monitored MRM transitions for relative metabolite quantification. All tables containing peak areas of detected metabolites were processed and filtered based on the coefficient of variation (CV) calculated across quality control (QC) samples. Data was discarded when peaks showed analytical variability with a CV above 30%. False discovery rate (FDR) correction was performed using the Benjamini, Krieger and Yekutieli method. Metabolites with FDR < 1% were loaded on MetaboAnalyst 6.0 for Pathway Impact Analysis using the Homo sapiens KEGG pathway library.[28] Both metabolite abundance and Pathway Impact Analysis results were plotted using Prism (GraphPad Software). All data is accessible via the Zenodo repository with dataset identifier 14002048.

NADH and NAD^+ quantification

DMEM lacking glucose, glutamine, phenol red and sodium pyruvate (Gibco, A14430) was supplemented with 10% dialyzed FBS, 100 U/mL penicillin/streptomycin and 25 mM glucose. K562 cells were seeded at 5-6 x 10^5/ml and supplemented with both 2 mM L-glutamine and 2 mM sodium pyruvate, only glutamine or pyruvate, or neither. Cells were cultured for 24 h and the medium was refreshed 5 h before sample collection. Cell pellets were prepared by flash-freezing pellets in liquid nitrogen, and intracellular metabolites were extracted by adding a mixture of 40% methanol, 40% acetonitrile, 20% LC-MS grade water containing 0.1 M formic acid. Samples were vortexed briefly, incubated on ice for 10 min and neutralized by adding 124 mM ammonium bicarbonate.

NADH and NAD^+ quantification was performed at Northeastern University (Boston, MA). Cell extracts were maintained at 4 °C in the autosampler prior to analysis. LC–MS experiments were performed on a Vanquish UHPLC system coupled to an Orbitrap Exploris 480 mass spectrometer (ThermoFisher). Chromatographic separations were carried out on a ZIC-pHILIC column (2.1 x 150 mm; Sigma-Aldrich, 1.50460.0001). The ZIC-pHILIC method was initiated at a flow rate of 0.15 mL min^{-1}, with the column temperature held at 30 °C and the initial mobile-phase B composition at 80% for 0.5 min. From 0.5 to 20.5 min, the gradient was maintained at 20% mobile-phase B at the same flow rate and held until 21.3 min. The column was then re-equilibrated at 0.15 mL min^{-1} and 80% mobile-phase B from 21.3 to 21.5 min.

The mass spectrometer was operated in SIM mode at a resolution of 60,000 with an m/z scan range of 600–850 in negative ion mode. The H-ESI ion source was used with static spray voltages of 3200 V (positive) and 2800 V (negative). Gas settings were as follows: sheath gas, 35 arb; auxiliary gas, 5 arb; sweep gas, 1 arb. The ion transfer tube temperature was set to 320 °C, and the vaporizer temperature was set to 175 °C.

NADH and NAD$^+$ chromatographic traces for each replicate were evaluated in Freestyle (ThermoFisher) to assess peak-shape quality, and peak areas were extracted in Freestyle for downstream quantification.

^{13}C-pyruvate isotopic profiling

K562 and primary murine CD8$^+$ T cells (7 days post-stimulation) were seeded at 5 x 10^5/mL in their respective media (supplemented with either 2 mM glutamine or water, for glutamine deprivation studies) and cultured for 16 h under standard culture conditions (37 °C, 5% CO_2) to allow for adaptation. Cells were then re-seeded at 5 x 10^5/mL in glucose-rich DMEM (K562) or RPMI (T cells) containing 10 % dialyzed FBS, 100 U/mL penicillin/streptomycin (K562) or 10 % dialyzed FBS, 100 U/mL penicillin/streptomycin, 50 μM β-mercaptoethanol (PAN Biotech, P07-05020) and 100 U/mL murine IL-2 (ThermoFisher/Gibco, 212-12) (T cells), and either supplemented with 2 mM glutamine (glutamine-rich conditions) or water (glutamine deprivation). 2mM ^{13}C-pyruvate ($^{13}C_3$-pyruvic acid, Omicron Biochemicals) was added to all samples, and cells were cultured at 37 °C, 5% CO_2 for 5 h (K562) or 4 h (T cells). Samples were centrifuged and frozen in liquid nitrogen before further processing.

For K562 cells, ^{13}C-pyruvate isotopic profiling was performed at the Metabolomics Platform at the University of Lausanne. Cell extracts were prepared and quantified as above (see "Multiple pathway targeted analysis of polar metabolites") and analyzed using Hydrophilic Interaction Liquid Chromatography coupled to high resolution mass spectrometry (HILIC-HRMS) in negative ionization mode with a 6550 Quadrupole Time-of-Flight (Q-TOF) system interfaced with a 1290 UHPLC system (Agilent Technology), as detailed elsewhere.[97] Metabolite separation was achieved via an iHILIC-(P) Classic PEEK column (100 x 2.1 mm, 5 μm particle size, HILICON AB, Umea, Sweden) column. Mobile phase composition was A = 20 mM ammonium acetate and 20 mM NH_4OH in water at pH 9.7 and B = 100% ACN. Linear gradient elution: 90% B (0-1.5 min) to 50% B (8-11 min) down to 45% B (12-15 min). For column re-equilibration, the initial chromatographic conditions were set during 9 min post-run (flow rate 300 μL/min, column temperature 30°C, injection volume 2 μL). ESI conditions were the following: dry gas temperature 290°C and flow 14 L/min, fragmentor voltage 380 V, sheath gas temperature 350°C and flow 12 L/min, nozzle voltage 0 V, and capillary voltage -2000 V. Acquisition was set over the full *m/z* range 50-1000 at the MS acquisition rate of 2 spectra/s. All ion fragmentation (AIF) MS/MS analysis was performed on pooled QC samples (collision energy 0, 10, 30 eV).

An *in-house* database containing 600 polar metabolites was employed for metabolite annotation, using the Profinder B.08.00 software (Agilent Technologies) and targeted data mining in isotopologue extraction mode. The METLIN standard spectral library was used to validate putative metabolite identity via the MS/MS fragmentation pattern,[98] and EICs were used for relative metabolite quantification. Natural isotype abundance was corrected in ProFinder.[99] All tables and peak areas of detected metabolites were exported to R (http://cran.r-project.org/), and signal intensity drift correction was performed with the LOWESS/Spline normalization algorithm,[100] followed by noise filtering (CV pooled sample > 30%).

^{13}C enrichment was calculated by taking into account the relative isotopologue abundances in two or more conditions as previously described.[101,102] Statistical significance was evaluated by applying univariate analysis on $\log_{10}$-transformed data, using a p-value set arbitrarily to 0.05, followed by false discovery rate correction (Benjamini-Hochberg). ^{13}C-pyruvate isotopic data in K562 are accessible via the Zenodo repository with dataset identifier 14002048, while ^{13}C-pyruvate isotopic data in primary CD8$^+$ T cells are accessible via the MetaboLights repository with dataset identifier MTBLS13799.

For primary murine CD8$^+$ T cells, ^{13}C-pyruvate isotopic tracer profiling was performed at Northeastern University (Boston, MA), and the extracts were analyzed using the ZIC-pHILIC LC–MS method described above (see NADH and NAD$^+$ quantification). Quantification was performed using Skyline (University of Washington).

^{13}C-glutamine and ^{15}N-glutamine isotopic profiling

^{13}C-glutamine and ^{15}N-glutamine isotopic profiling was performed at Northeastern University (Boston, MA). K562 cells were maintained under standard culture conditions (37 °C, 5% CO_2) and cultured in DMEM lacking D-glucose, L-glutamine, and phenol red, supplemented with 10% FBS (ThermoFisher), 1% of a 25 μg/mL stock antibiotic–antimycotic solution (Cytiva), 25 mM glucose (ThermoFisher), and 2 mM sodium pyruvate (ThermoFisher).

For tracer studies, 2 mM unlabeled glutamine (Corning), ^{13}C-glutamine (99% $^{13}C_5$; Cambridge Isotope Laboratories) or ^{15}N-glutamine (98% $^{15}N_2$; Cambridge Isotope Laboratories) were prepared in cell culture-grade water. A time-course experiment was conducted with the following sampling intervals: 0, 0.5, 1, 2, 4, 8, and 24 h for the unlabeled control, and 0.5, 1, 2, 4, 8, and 24 h for the ^{13}C- and ^{15}N-tracer groups. For each time point, three biological replicates were seeded in freshly prepared cell tracer medium at a density of 5 x 10^5/mL.

For metabolite extraction, 800 μL of cell suspension was collected from each well at the designated time point and pelleted at 400 *g* for 5 min at room temperature. Samples were extracted with 300 μL of ice-cold extraction solvent (40% methanol, 40% acetonitrile, 20% LC–MS grade water) containing 0.1 M formic acid. Samples were kept on ice for 10 min, then neutralized with 124 mM ammonium bicarbonate. Extracts were subsequently analyzed using the ZIC-pHILIC LC-MS method, as described for NADH/NAD$^+$ quantification. Quantification data was performed by Skyline (University of Washington). All data are accessible via the MetaboLights repository with dataset identifier MTBLS13799.

Please cite this article in press as: Lisci et al., Functional nutrient-genetic profiling reveals biotin and FBXW7 are essential to bypass glutamine addiction, Molecular Cell (2026), https://doi.org/10.1016/j.molcel.2026.02.002

QUANTIFICATION AND STATISTICAL ANALYSIS

Values are presented as mean ± SD (technical repeats) of one representative experiment from at least three biological replicates, except for mRNA decay, MAX and SIN3A ChIP experiments, which show one representative dataset from two biological replicates. Fitted curves for ^{13}C-glutamine and ^{15}N-glutamine tracing experiments were calculated by non-linear regression (one-phase association model). Statistical significance was calculated by two-sided Student's t-test or ANOVA as specified in the figure legends, and exact p-values are shown when lower than $p < 0.05$. All graphs were generated using Prism 10 (GraphPad Software).

Molecular Cell, Volume *86*

Supplemental information

Functional nutrient-genetic profiling reveals biotin and FBXW7 are essential to bypass glutamine addiction

Miriam Lisci, Fanny Vericel, Yifan Liu, Hector Gallart-Ayala, Julijana Ivanisevic, Owen S. Skinner, and Alexis A. Jourdain

Molecular Cell, Volume *86*

Supplemental information

Functional nutrient-genetic profiling reveals biotin and FBXW7 are essential to bypass glutamine addiction

Miriam Lisci, Fanny Vericel, Yifan Liu, Hector Gallart-Ayala, Julijana Ivanisevic, Owen S. Skinner, and Alexis A. Jourdain

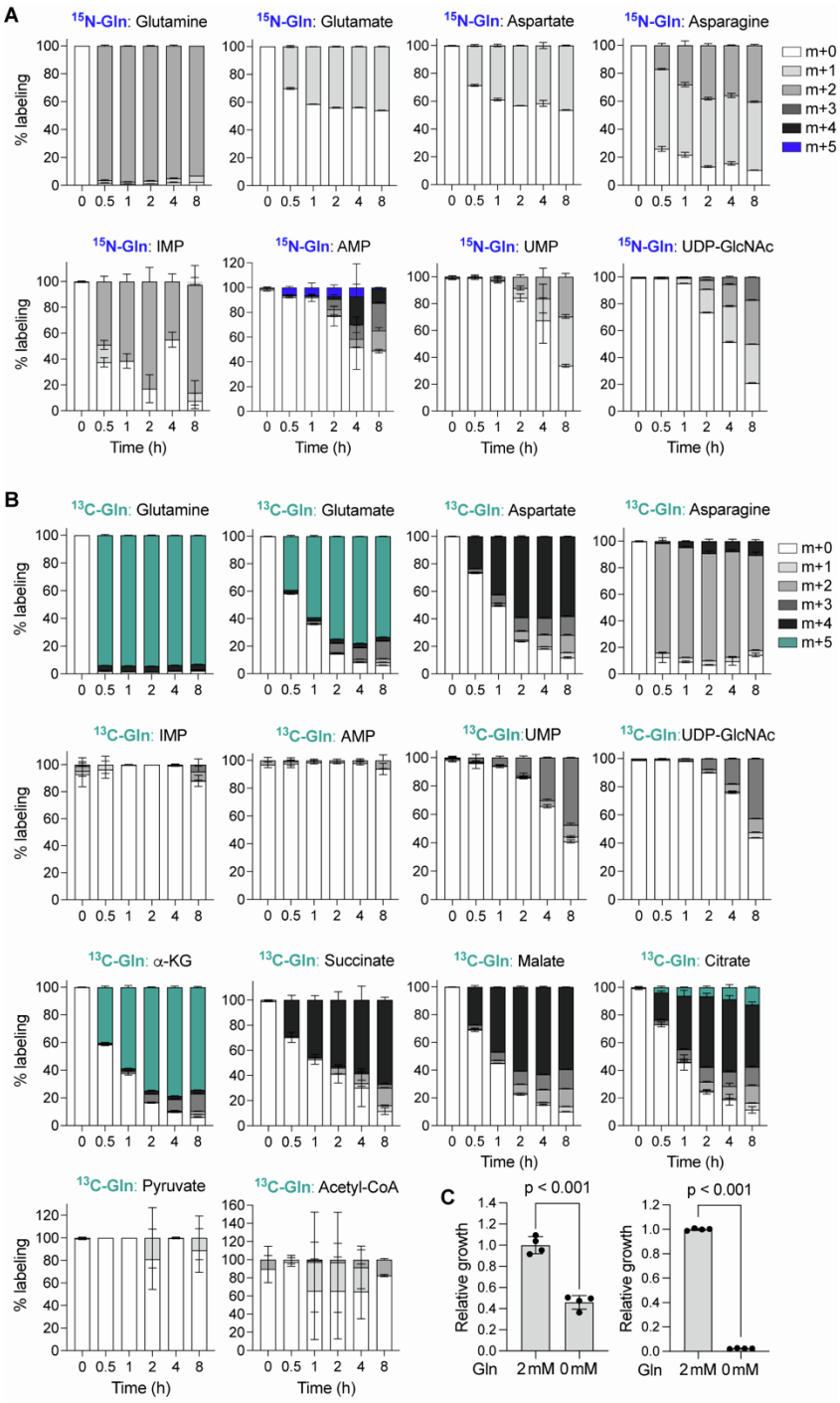

Figure S1. Individual isotopologues for ^{15}N- and ^{13}C-glutamine tracers and additional assays used to quantify cell viability and proliferation, related to Figure 1.

(A, B) Individual isotopologues for ^{15}N-glutamine (A) and ^{13}C-glutamine (B) for glutamine, glutamate, aspartate, asparagine, IMP, AMP, UMP, UDP-GlcNac, α-KG, succinate, malate and citrate curves shown in Figure 1. Results from ^{13}C-glutamine labeling of pyruvate and acetyl-CoA are provided at the bottom. **(C)** CellTiter-Glo-based (left) and cell count-based (right) growth assays of K562 cells in medium with or without glutamine (Gln). p-values: unpaired t-test. Relative growth is calculated as fold change of cell proliferation in medium containing glutamine. All data are represented as mean ± SD.

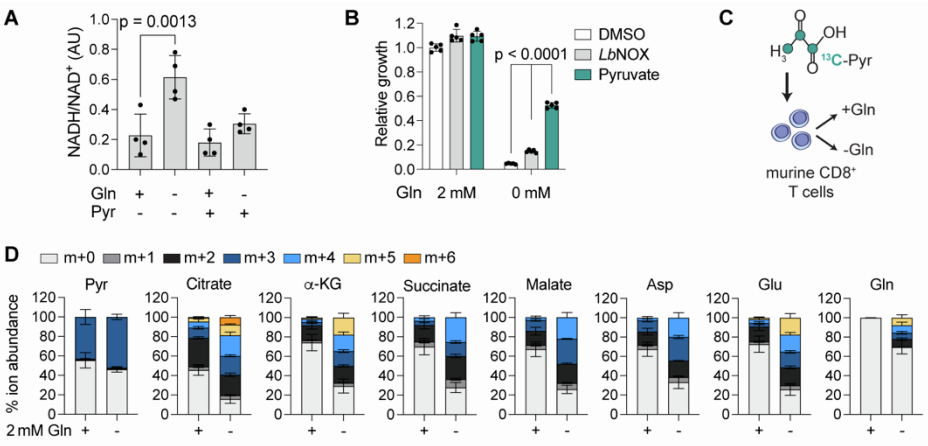

Figure S2. NADH/NAD$^+$ quantification, proliferation of *Lb*NOX-overexpressing K562, and ^{13}C-pyruvate tracer in primary CD8$^+$ T cells, related to Figure 2.

(A) NADH/NAD$^+$ quantification in wild-type K562 cells cultured in medium that was either enriched or deprived of glutamine (Gln) or pyruvate (Pyr) as indicated. AU: alternative units. **(B)** Proliferation of K562 cells in medium either enriched or deprived of glutamine. Cells were either expressing *Lb*NOX or cultured in the presence of pyruvate. Relative growth refers to fold change based on proliferation of control cells cultured in glutamine-rich medium (2 mM), with no pyruvate or *Lb*NOX added. **(C)** ^{13}C-pyruvate tracing strategy in primary murine CD8$^+$ T cells. **(D)** Metabolites enriched in ^{13}C-pyruvate in glutamine-rich and glutamine-deprived medium, showing relative fractions of isotopologues within each metabolite. Pyr: pyruvate; α-KG: α-ketoglutarate; Asp: aspartate; Glu: glutamate; Gln: glutamine. All data are represented as mean ± SD. All p-values: one-way ANOVA.

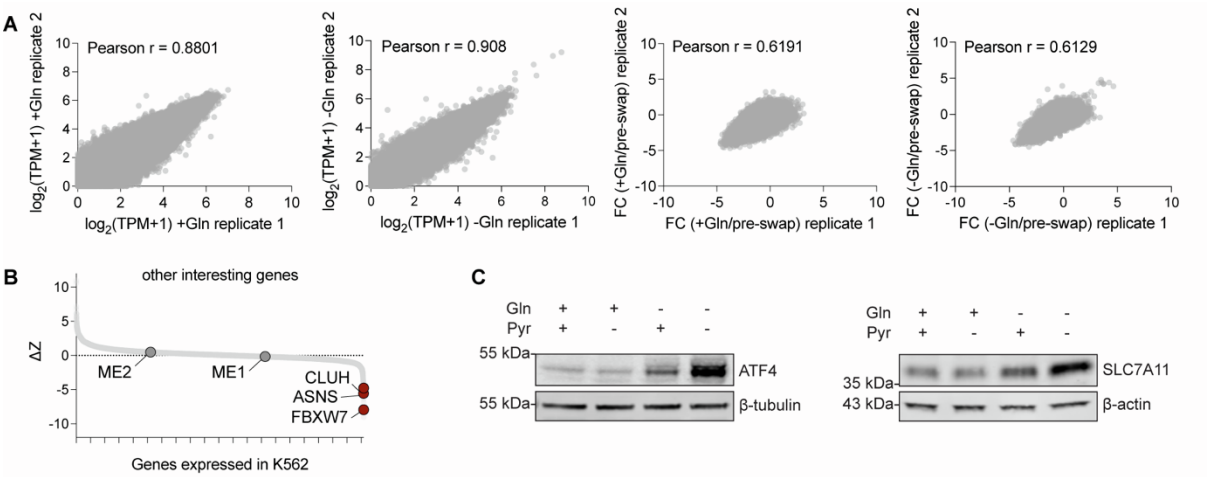

Figure S3. Additional data for CRISPR-Cas9 screen reproducibility and validation, related to Figure 3.

(A) CRISPR reproducibility plots. FC: fold change. TPM: Transcripts per million. Gln: glutamine. **(B)** Gene essentiality score ($\Delta Z = Z_{-Gln} - Z_{+Gln}$) for additional hits identified in the CRISPR-Cas9 screen. Genes required to promote proliferation of glutamine-starved cells (supplemented with pyruvate) are labeled in red ($\Delta Z<-2$), while genes that scored below our threshold (detrimental $\Delta Z>2$; required: $\Delta Z<-2$) are labeled in grey. **(C)** Immunoblots showing ATF4 (left) and SLC7A11 (right) expression upon depletion of glutamine (Gln), pyruvate (Pyr) or both.

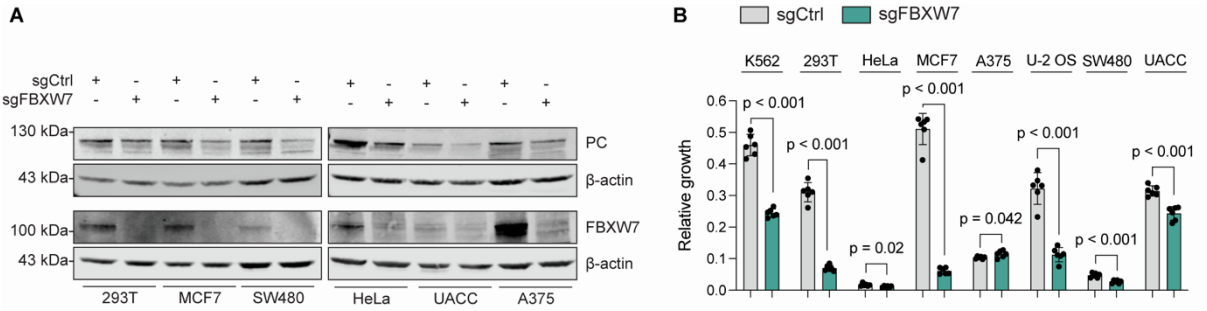

Figure S4. Loss of *FBXW7* leads to PC downregulation in multiple cell lines, related to Figure 5.

(A) Immunoblot showing PC and FBXW7 expression across 6 human cancer cell lines depleted of *FBXW7* using CRISPR-Cas9. **(B)** Growth assay of *FBXW7*-depleted cell lines in medium enriched with 2 mM pyruvate and depleted of glutamine. Relative growth shows values as fold change of growth of the same cell line in glutamine-rich medium. All data are represented as mean ± SD. p-values: multiple unpaired t-tests.

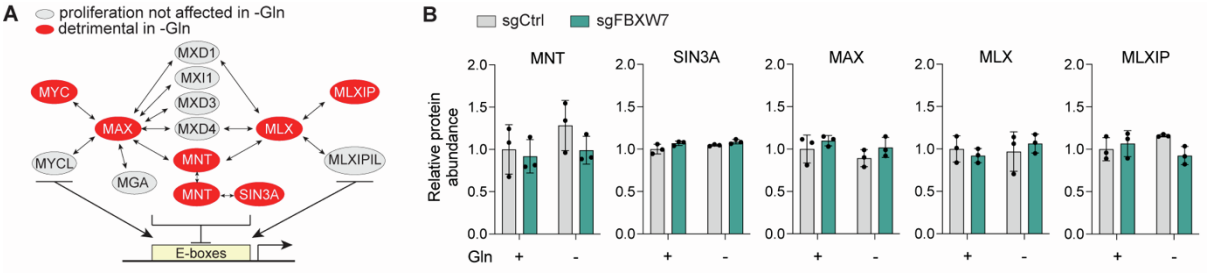

Figure S5. Additional data on the *MYC* extended network, related to Figure 6.

(A) Summary of the MYC extended network, adapted from PMIDs: 28230739; 34572909. Genes that scored as essential for promoting proliferation upon glutamine (Gln) restriction are highlighted by red ellipses. Genes that scored below threshold did not affect proliferation and shown within grey ellipses. **(B)** Proteomic analysis of MNT, MAX, MLX and MLXIP abundance in glutamine-enriched compared to glutamine-deprived sgCtrl and sgFBXW7 cells. Relative protein abundance is calculated as a fold change of protein abundance in sgCtrl cells in glutamine-rich medium. All data are represented as mean ± SD.